


RESEARCH ARTICLE

Modelling and parametrization of the convective flow over leads in sea ice and comparison with airborne observations

Janosch Michaelis¹  | Christof Lüpkes¹ | Amelie U. Schmitt² | Jörg Hartmann¹

¹Alfred Wegener Institute Helmholtz Centre for Polar and Marine Research, Bremerhaven, Germany

²University of Hamburg, Hamburg, Germany

Correspondence

J. Michaelis, Climate Sciences, Alfred Wegener Institute, Am Handelshafen 12, 27570 Bremerhaven, Germany.
Email: janosch.michaelis@awi.de

Funding information

Deutsche Forschungsgemeinschaft (DFG, German Research Foundation) via the Transregional Collaborative Research Center ArctiC Amplification (AC)3 (project number 268020496 TRR 172) and via the priority program SPP 1158 (grant LU 818/5-1)

Abstract

A non-eddy-resolving microscale model is applied to simulate convection over three different leads (elongated channels in sea ice), which were observed by aircraft over the Arctic Marginal Ice Zone in 2013. The study aims to evaluate the quality of a local and a non-local turbulence parametrization. The latter represents a lead-width-dependent approach for the turbulent fluxes designed for idealised conditions of a lead-perpendicular, near-neutral inflow in an atmospheric boundary layer (ABL) capped by a strong inversion at around 250 to 350 m height. The observed cases considered here are also characterised by an almost lead-perpendicular flow but, in comparison to the idealised conditions, our analysis covers effects in stable inflow conditions and a much shallower ABL. The model simulations are initialised with observed surface parameters and upwind profiles, and the results are compared with measurements obtained above and downwind of the leads. The basic observed features related to the lead-generated convection can be reproduced with both closures, but the observed plume inclination and vertical entrainment near the inversion layer by the penetrating plume are underestimated. The advantage of the non-local closure becomes obvious by the more realistic representation of regions with observed vertical entrainment or where the observations hint at counter-gradient transport. It is shown by comparison with the observations that results obtained with the non-local closure can be further improved by including the determination of a fetch-dependent inversion height and by specifying a parameter determining the plume inclination as a function of the upwind ABL stratification. Both effects improve the representation of fluxes, boundary-layer warming, and vertical entrainment. The model is also able to reproduce the observed vanishing of a weak low-level jet over the lead, but its downwind regeneration and related momentum transport are not always well captured, irrespective of the closure used.

KEYWORDS

aircraft observations, atmospheric boundary layer, convection over leads, counter-gradient transport, entrainment, microscale model, sea ice, turbulence parametrization

This is an open access article under the terms of the Creative Commons Attribution-NonCommercial License, which permits use, distribution and reproduction in any medium, provided the original work is properly cited and is not used for commercial purposes.

© 2020 The Authors. *Quarterly Journal of the Royal Meteorological Society* published by John Wiley & Sons Ltd on behalf of the Royal Meteorological Society.

1 | INTRODUCTION

Elongated open-water channels in sea ice, so-called leads, may play a key role for surface–atmosphere interactions in the polar regions (e.g., Ebert and Curry, 1993; Lüpkes *et al.*, 2008b; Vihma *et al.*, 2014; Chechin *et al.*, 2019). Over these areas, the atmosphere is in direct contact with open water or nilas, which leads to an enhanced heat transport, especially during wintertime when temperature differences between atmosphere and open water are large. This, in turn, generates several effects on the characteristics of the polar atmosphere on different (spatial) scales.

As described, for example, in the above-mentioned studies and most recently by Michaelis *et al.* (2020, henceforth M20), leads are formed mainly by divergent sea ice drift driven by ocean currents and wind (also Smith *et al.*, 1990). Their length ranges between hundreds of metres and hundreds of kilometres and their width between a few metres to a few kilometres (e.g., Andreas *et al.*, 1979; Smith *et al.*, 1990; Lindsay and Rothrock, 1995; Marcq and Weiss, 2012; Tetzlaff *et al.*, 2015, henceforth T15). Leads occur predominantly in the marginal ice zone (MIZ), but they are also found in the central polar ocean regions (Smith *et al.*, 1990). Due to the above-mentioned large temperature difference in wintertime, the heat transport through leads exceeds the molecular heat transport through the surrounding thick ice by two orders of magnitude (Badgley, 1966; Maykut, 1978) so that leads can dominate the heat budgets even if the lead coverage is only a few percent (Maykut, 1978; Smith *et al.*, 1990). Thus, strong turbulent convection (convective plumes) and an internal boundary layer (IBL) are generated, which strongly affect the structure of the polar atmospheric boundary layer (ABL). The intensity of those effects depends on the lead geometry and the meteorological forcing (temperature, wind speed and direction, and stratification). Furthermore, effects generated over multiple leads or polynyas can have an impact also on the near-surface energy balance and on atmospheric processes at spatial scales up to 10^3 km (e.g., Overland *et al.*, 2000; Ebner *et al.*, 2011; Batrak and Müller, 2018; Chechin *et al.*, 2019). This shows the relevance of leads for climate and numerical weather prediction, especially in high latitudes.

Investigating the effects of leads on the polar ABL has been subject of many studies using observations, numerical models, or both. During the campaigns AID-JEX (Arctic Ice Dynamics Joint Experiment; Paulson and Smith, 1974; Andreas *et al.*, 1979), LEADDEX (Leads Experiment; Ruffieux *et al.*, 1995; Persson *et al.*, 1997, and SHEBA (Surface Heat Budget of the Arctic Ocean; Overland *et al.*, 2000; Persson *et al.*, 2002; Pinto *et al.*, 2003, near-surface atmospheric processes near leads were

analysed in detail using mainly *in situ* measurements. Based on those measurements, turbulent surface fluxes of heat, moisture, and momentum had been derived and parametrizations for the corresponding transfer coefficients were proposed (e.g., Andreas and Murphy, 1986; Alam and Curry, 1997; Andreas and Cash, 1999). All studies revealed a strong influence of lead-generated convection on the near-surface ABL.

During the Winter Arctic Polynya Study (WARPS; Lüpkes *et al.*, 2004; Lüpkes *et al.*, 2012), additional *in situ* measurements were also performed above leads, supplemented by helicopter-borne turbulence measurements with the HELIPOD system (Bange *et al.*, 2002). Thus, one of the main shortcomings during previous campaigns with measurements only over sea ice had been overcome. Unlike during LEADDEX and SHEBA, the focus was mainly on leads of width $L = \mathcal{O}(10^3)$ m rather than $L = \mathcal{O}(10^1 - 10^2)$ m. In March 2013, detailed observations of the whole turbulent ABL over leads similar in width to those during WARPS were performed during the aircraft-based Spring-Time Atmospheric Boundary Layer Experiment (STABLE; T15). Measurements from STABLE revealed that, for convection penetrating the capping inversion, not only the surface heat fluxes but also fluxes entrained through the inversion significantly contribute to the warming of the ABL (T15).

Lead-generated convection was also subject of several modelling studies using either large-eddy simulation (LES; e.g., Glendening and Burk, 1992; Glendening, 1994; Weinbrecht and Raasch, 2001; Esau, 2007), high-resolved non-hydrostatic models (e.g., Alam and Curry, 1995; Dare and Atkinson, 2000; Zulauf and Krueger, 2003a; 2003b; Mauritsen *et al.*, 2005; Wenta and Herman, 2018; Li *et al.*, 2020), or both (e.g., Lüpkes *et al.*, 2008a, henceforth L08, and M20). Most of these studies focused on idealised case-studies to analyse the impact of lead geometry and meteorological forcing on the convective ABL. LES models provide detailed information on the turbulence structure since the energy-contributing turbulent scales are directly resolved. Typically, grid sizes of the order of a few metres or less are used in all directions, with the resolution having increased in recent years due to increased computer capacity. The computational costs of a non-eddy-resolving model amount to only 0.1–1% of an LES model due to the much coarser resolution ($\mathcal{O}(10^2 - 10^3)$ m horizontally and $\mathcal{O}(10^1)$ m vertically), but if the latter is appropriate, the main characteristics of the developing plume can still be provided. However, parametrizations of the dominating subgrid-scale processes are required so that the simulation results strongly depend on the applied closure. Among others, the above-mentioned modelling studies all showed the formation of convective plumes over single leads or polynyas with distinct upper and lower boundaries and a

significant influence on temperature and wind patterns of the ABL.

The parametrizations applied in the non-LES applications predominantly follow local turbulence closures (1.5-, 2-, or 2.5-order turbulent kinetic energy (TKE) schemes). However, for example, Dearnorff (1972) and Holtslag and Moeng (1991) found fluxes directed against the prevailing temperature gradient, especially in the upper half of a homogeneously surface-heated ABL. As stressed by L08 and M20 based on their LES results, such non-local fluxes dominate the heat flux pattern also in case of horizontally inhomogeneous convection over leads. Furthermore, the measurements from STABLE indicated that those fluxes exist. To account for non-local fluxes, L08 proposed a corresponding parametrization based on LES using K -theory with a counter-gradient correction for leads of 1 km width. They showed that for such cases, non-eddy-resolving model results obtained with their non-local parametrization agree well with their LES results. The basic idea of L08 was also used by M20, who modified and extended the non-local parametrization but accounted additionally for variable lead width. As compared with the local and the previous non-local closure, a considerably improved agreement with LES was obtained, especially concerning heat flux patterns and downstream stratification for wide leads with $L \geq 5$ km.

M20 considered idealised cases with neutral stratification and only with a fixed ABL height at $z_i = 300$ m. Neither non-neutral upstream stratification, nor other values for z_i , nor observed leads were investigated. Furthermore, as T15 showed, values for z_i up- and downstream of the lead might differ due to interactions caused by penetrating convection. This phenomenon was also not captured by the M20 parametrization since z_i was kept constant.

The aim of this paper is, first of all, to discuss the quality of microscale model results using different turbulence closures, with a focus on the M20 parametrization, when applied to the cases observed during STABLE. The first leading question is whether the non-local closure has advantages as compared to a simpler local closure. We investigate three out of the four cases, all of them with a shallower ABL and two of them with a more stable upwind stratification than the idealised cases considered by M20. The fourth case from STABLE is not modelled due to a rather complex distribution of sea ice cover and surface temperatures.

Another goal is to investigate the need for possible modifications of the M20 parametrization based on the comparison with the measurements. This includes the consideration of ABL warming caused by convection penetrating the capping inversion and of the impact of non-neutral stratification on the plume inclination. A consideration of the latter effect is, furthermore, motivated by

analytical models proposed for the IBL developing over heated surfaces, where a functional relation to the upwind temperature gradient was proposed (e.g., Weisman, 1976; Renfrew and King, 2000). All this can be regarded as another step towards a turbulence parametrization for convective processes in strongly inhomogeneous conditions used in non-eddy-resolving but small-scale atmospheric models.

In Section 2, we describe the campaign STABLE followed by the description and set-up of the applied microscale model in Section 3. Model results obtained with different turbulence closures are shown and compared with the observations in Section 4. Based on those model results, in Section 5 we introduce two further modifications for the non-local parametrization followed by the corresponding results. A discussion is given in Section 6, and conclusions are drawn in Section 7.

2 | THE STABLE CAMPAIGN

In the following, we briefly summarise the campaign STABLE with focus on the three cases considered here and on information relevant for our simulations. T15 give more details on the observations, flight patterns, and measurement techniques, and a detailed discussion on observed ABL effects by the leads.

STABLE was an aircraft campaign with focus on measurements over leads conducted in the MIZ north of Svalbard in March 2013. Measurements were conducted over four leads (on 10, 11, 25, and 26 March) using the Polar 5 research aircraft from the Alfred Wegener Institute in Germany. Temperature, wind components, and pressure were measured with a frequency of 100 Hz, which is equivalent to measurements every 0.4 to 0.75 m during horizontal flight legs considering the aircraft's ground speed between 40 and 75 m·s⁻¹. Humidity was measured only with a frequency of 1 Hz, so that turbulent fluctuations could not be resolved. Upwind and downwind of the leads, ascending and descending profiles were performed, for example, to determine stratification and ABL height. Horizontal, lead-perpendicular flight legs were conducted predominantly at around 40 m height along the main wind direction, mainly to determine humidity, wind, and both surface and air temperature. On 11 and 25 March, flight sections following a vertical saw-tooth pattern in the lead-perpendicular direction were additionally performed to derive the vertical structure of the ABL. In the lead-parallel direction, several horizontal stacks were flown above and downwind of the leads (see below).

In all cases, the near-surface wind was approximately lead-perpendicular with an upstream ABL-averaged speed

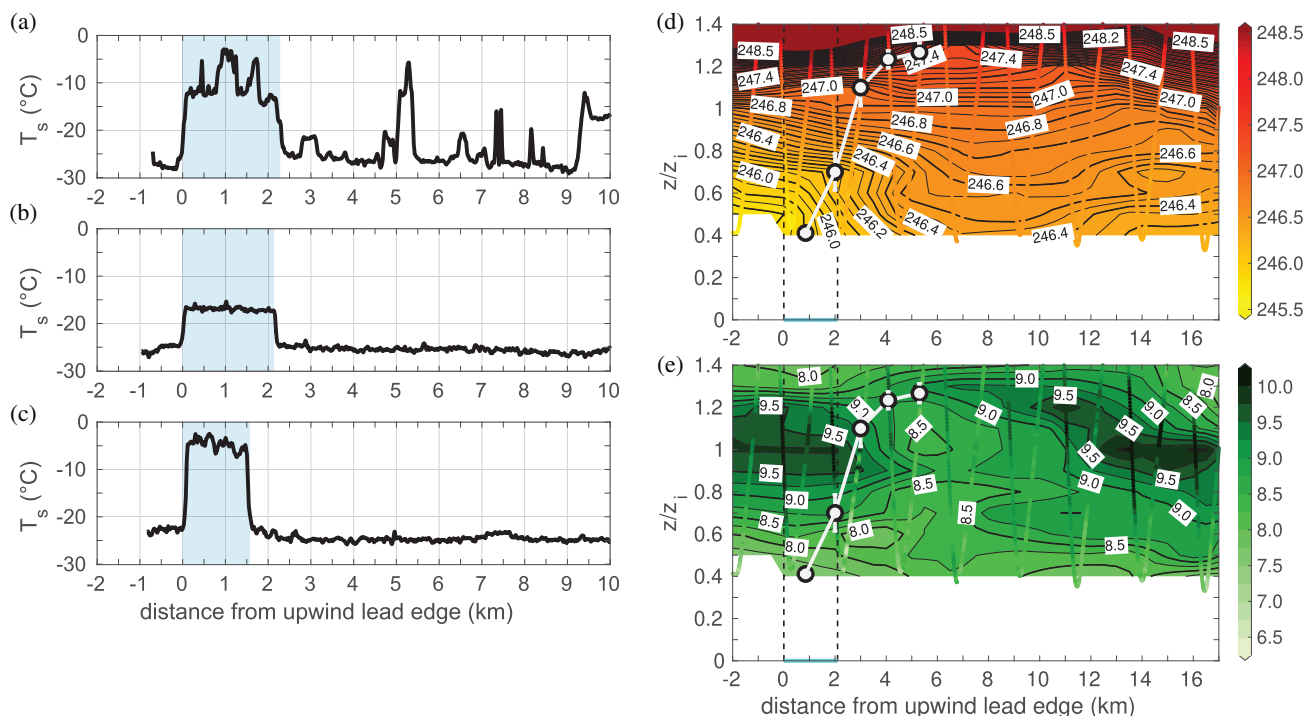


FIGURE 1 Observed surface temperature T_s against distance from the upwind lead edge for three lead cases from STABLE, where the position of the leads is denoted by the shaded rectangles: (a) lead of 2.3 km width observed on 10 March 2013, (b) lead of 2.1 km width observed on 25 March 2013, and (c) lead of 1.6 km width observed on 26 March 2013. Observations of (d) potential temperature (K) and (e) horizontal wind speed ($\text{m}\cdot\text{s}^{-1}$) in the lead-perpendicular direction were derived from the saw-tooth leg on 25 March 2013. Smoothed measurements are shown as dots and linear interpolation was applied for the filled contours using a method similar to T15. The observed upper IBL height is shown in white, based on figure 22b of T15. The lead edges are denoted by the vertical dashed black lines. The upwind observed ABL height is $z_i = 90$ m

U of 5.5 to 10.5 $\text{m}\cdot\text{s}^{-1}$ (T15; their table 1). Thus, inclined plumes developed over the leads, which extended into the downstream region over closed sea ice. The plumes also penetrated into the capping inversions above the shallow near-neutrally or stably stratified ABLs with $90 \text{ m} \leq z_i \leq 190 \text{ m}$. The surface temperature of thick sea ice around the leads was near -25°C and lead-averaged surface temperatures, $\overline{T}_{s,l}$, ranged from -17°C to -5°C , partly with large spatial variations due to different surface cover (Figure 1). The widths of the leads, L , ranged from 1.6 to 8.3 km.

As shown in more detail by T15, during STABLE, much attention was paid to an optimal measurement strategy to obtain reliable turbulent fluxes by applying the following rules. First, fluxes were derived only from flight sections parallel to the lead orientation and not from legs in the lead-perpendicular direction. This method allowed flight legs of sufficient length (around 5 to 15 km) for an application of the eddy covariance method. The statistical error of the measurements is discussed in detail by T15 (their section 4). Considering the above-mentioned ABL depths, the leg lengths were about 10 to 50 times

the plume size. Thus, local disturbances (e.g., by individual plumes or thermals), had been filtered out. Second, horizontal flight legs for fluxes had always sufficient distance from each other (at least about 1 km) so that potential differences between results of two legs can be considered as non-random. Mostly, one leg was flown at the lead's centre, another one at the lead's downstream edge, and, partly, further legs further downwind. Third, the focus was on lead sections almost without any curved structures. The uncertainty of the fetch (the distance between the upwind lead edge and a single lead-parallel flight leg) by the remaining small-scale curvature of lead edges was corrected by filtering (T15 give details).

All leads were covered with nilas except of some small patches of open water. Thus, the average lead surface temperatures were far below the temperature of open water (Figure 1) so that the sensible heat fluxes were smaller than over an ice-free lead. Since the nilas cover strongly reduces evaporation compared with open water (Li *et al.*, 2020), cloud formation over the leads was prevented.

2.1 | 10 March 2013

The lead observed on 10 March was 2.3 km wide with a neutrally stratified ABL up to $z_i = 95$ m upwind of the lead (at $y = -7$ km, where y is the distance to the upwind lead edge at $y = 0$ km). T15 found that the observations derived from this flight leg were not completely representative for the conditions directly in front of the lead due to another narrow lead further upwind. Hence, for example, air temperatures above the lead were lower than at $y = -7$ km over thick sea ice (T15; their figure 5a).

The lead was mostly covered by thin ice (grey nilas), whose average surface temperature amounted to $\overline{T}_{s,l} = -10.7^\circ\text{C}$, but some patches of just refreezing open water with $T_{s,l} \approx -3^\circ\text{C}$ occurred also. This caused a large standard deviation of $\sigma_{T_{s,l}} = 3.9^\circ\text{C}$ in $T_{s,l}$ (Figure 1a). Above the open water areas, some sea smoke was present. The average temperature difference between the surfaces of thick sea ice and the lead amounted to approximately 14.8 K. An average wind speed of $U = 5.5 \text{ m}\cdot\text{s}^{-1}$ was derived based on the profile at $y = -7$ km. T15 found that the plume had also penetrated the capping inversion so that the ABL thickness had slightly increased from 95 m at $y = 0$ km to 101 m near $y = L$ where small entrainment fluxes had been observed. Due to lead-generated convection, mixed-layer air temperatures increased by approximately 0.8 K, where the maximum temperature increase was reached near $y = L$.

2.2 | 25 March 2013

On 25 March, the temperature difference between the surfaces of the lead ($L = 2.1$ km) and of the sea ice in the environment of the lead was smallest among all cases with only 8 K, where $\overline{T}_{s,l} = -17.0^\circ\text{C}$ and $\sigma_{T_{s,l}} = 0.4^\circ\text{C}$ (Figure 1b). These low values occurred due to the nilas cover of almost 100% except some small areas of grey nilas. The upwind ABL with $U = 8.0 \text{ m}\cdot\text{s}^{-1}$ was stably stratified with a vertical potential temperature gradient $\partial\theta/\partial z = 0.014 \text{ K}\cdot\text{m}^{-1}$ below the inversion at $z_i = 90$ m. Due to the shallow boundary layer, the lowest height reached by the aircraft was at $0.4z_i$. Thus, only a small part of the ABL structure is visible in the measurements (T15 and also Figures 1d,e).

Especially for this case, T15 found large vertical entrainment fluxes due to the inversion-penetrating plume and also the bottom of the inversion z_i had increased by 25 m to 115 m downwind of the lead. This increase is denoted also in Figures 1d,e by the observed upper plume boundary (T15 give the detailed determination of this quantity). Thus, the stable stratification had weakened above and downwind of the lead, which was derived by T15 based on a saw-tooth flight pattern across the lead

(Figure 1d). The mixed-layer temperature increased by approximately 0.6 K until $y = L$ and up to 1.2 K further downwind at $y = 8$ km. This indicates a large contribution by entrainment (T15). Furthermore, also based on the saw-tooth pattern, T15 found a low-level jet (LLJ) upwind of the lead with its maximum near z_i exceeding U by approximately $2 \text{ m}\cdot\text{s}^{-1}$, which had then been destroyed by the plume, and which had regenerated near $y = 15$ km downwind of the lead (Figure 1e).

2.3 | 26 March 2013

The lead observed on 26 March was the narrowest one ($L = 1.6$ km) and it had the highest surface temperature ($\overline{T}_{s,l} = -5.8^\circ\text{C}$; Figure 1c). The surface was mainly covered by nilas, but locally it also consisted of open water areas and frazil ice. $\sigma_{T_{s,l}} = 3.8^\circ\text{C}$ was almost as large as on 10 March and also on that day weak sea smoke was present above the open water areas. However, there were no such clear peaks in $T_{s,l}$ as on 10 March. The upwind ABL was less stable ($\partial\theta/\partial z = 0.003 \text{ K}\cdot\text{m}^{-1}$) and thicker ($z_i = 190$ m) than on 25 March. The highest altitude for the lead-parallel horizontal flight legs was at 140 m so that no measurements were obtained near z_i , which did not allow us to identify an effect of a growing ABL height downwind of the lead. However, the potential impact of convection on the capping inversion was observed indirectly by measured intermittency of the turbulence in the inversion over the plume region, which had been present also in the other cases.

3 | MODEL DESCRIPTION

For our simulations, we use the mesoscale atmospheric model METRAS (MEsoscale Transport and Stream Model; Schlünzen *et al.*, 2012a; 2012b), which is run with a turbulence closure that allows also microscale but non-eddy-resolving resolution as explained below. METRAS is a non-hydrostatic and anelastic model and is applied here in the same 2D version as described by both L08 and M20.

The Boussinesq-approximated model equations of METRAS are solved on a staggered Arakawa-C grid with a horizontal grid spacing of 100 m. In the vertical direction, an equidistant grid spacing of 20 m is applied in the ABL. Further above, a non-equidistant grid spacing is used up to the model's top, which is near 9,600 m, ensuring that gravity waves are damped towards the model's top.

Following L08 and M20, we use the idealised dry model version and account for radiation only implicitly due to its impact on the inflow profile and on the prescribed surface

temperature resulting in nature from all processes contributing to the surface energy budget. Humidity is considered but without phase transitions, which is justified due to the absence of clouds in the cases considered (T15).

Fixed values are prescribed for temperature and humidity at the inflow boundary. For the outflow boundary, we use the same conditions as M20. The treatment of outflow boundaries in METRAS is explained by Schlünzen *et al.* (2012a; 2012b).

3.1 | Turbulence parametrizations

As explained in detail by M20, the turbulence parametrization is one of the most important model features for simulations on the microscale. Due to the grid size applied here in METRAS, we assume that turbulent transport is entirely captured as a subgrid-scale and thus parametrized process. We apply two different closure schemes for turbulence, a local mixing-length closure and a non-local closure accounting for the inhomogeneous convection over leads of different width. In the following, we summarise these parametrizations as used here, based on the detailed description of M20.

3.1.1 | Local closure

The applied local closure scheme of Herbert and Kramm (1985) is based on flux-gradient relationships

$$\overline{w'\theta'} = -K_h \frac{\partial \bar{\theta}}{\partial z}, \quad (1)$$

for temperature, where $\partial \bar{\theta} / \partial z$ is the vertical potential temperature gradient and K_h is the eddy diffusivity for heat, and

$$\overline{w'u'} = -K_m \frac{\partial \bar{u}}{\partial z}, \quad \overline{w'v'} = -K_m \frac{\partial \bar{v}}{\partial z}, \quad (2)$$

for momentum, where $\partial \bar{u} / \partial z$ and $\partial \bar{v} / \partial z$ are the vertical gradients of the x - and y -components of the wind vector and K_m is the eddy diffusivity for momentum. Latent heat fluxes are not part of our study since they were also not analysed by T15. Thus, we will use the term heat flux for sensible heat fluxes, unless stated otherwise.

For both closure schemes applied here, in the surface layer (first grid cell above the surface), both K_m and K_h are calculated according to Monin–Obukhov similarity theory using Businger–Dyer functions (Businger *et al.*, 1971; Dyer, 1974). Above the surface layer, the calculation of K_m and K_h in Equations (1) and (2) follows a mixing-length approach as formulated by Herbert and Kramm (1985), so

that

$$K_m = \begin{cases} l_n^2 \left| \frac{\partial \mathbf{v}_h}{\partial z} \right| (1 - 5Ri)^2 & \text{for } 0 \leq Ri \leq Ri_c \\ l_n^2 \left| \frac{\partial \mathbf{v}_h}{\partial z} \right| (1 - 16Ri)^{1/2} & \text{for } Ri < 0, \end{cases} \quad (3)$$

$$K_h = \begin{cases} K_m & \text{for } 0 \leq Ri \leq Ri_c \\ K_m(1 - 16Ri)^{1/4} & \text{for } Ri < 0, \end{cases} \quad (4)$$

where Ri is the Richardson number and Ri_c is the critical Richardson number. Unlike the original formulation by Herbert and Kramm (1985), we apply $Ri_c = 0.199$ instead of $Ri_c = 0.2$ to avoid zero diffusion. $\partial \mathbf{v}_h / \partial z$ is the vertical gradient of the horizontal wind and $l_n = \kappa z / (1 + \kappa z / l_{\max})$ is the mixing length for neutral stratification with von Kármán's constant κ . For the determination of l_n , we follow L08 and M20 and set the maximum mixing length $l_{\max} = 0.15z_i$. Originally, this relation was derived by Brown (1996) based on LES. If $Ri > Ri_c$, both K_m and K_h are calculated with $Ri = Ri_c$ to guarantee matching with the surface layer when Businger–Dyer functions are used in the case of stable stratification. By applying Equations (3) and (4), continuous fluxes are guaranteed at the first grid level.

3.1.2 | Non-local closure of M20

Our analysis focuses on the application of a non-local closure developed by M20 for the microscale modelling of lead-generated convection. Their basic equation to parametrize heat fluxes is the flux-gradient relationship with a counter-gradient correction Γ (Equation (5)). This approach, which was first proposed by Priestley and Swinbank (1947) and theoretically derived by, for example, Holtslag and Moeng (1991) based on LES, captures also the counter-gradient fluxes. These fluxes are directed against the vertical gradient of the mean (grid-cell averaged) potential temperature. Lüpkes and Schlünzen (1996) improved the latter derivation and arrived at a formulation ensuring continuity of the fluxes at the top of the surface layer (z_p). Then, L08 transferred this approach to the inhomogeneous, microscale environment over a lead of 1 km width (as a starting point). In turn, M20 modified and extended that approach to account for different lead width L . The basic idea of L08 remained unchanged, namely to distinguish between the plume region with possible gradient-independent transport and its environment with only gradient transport (Figure 2), for which the above-mentioned local approach is used. The non-local parametrizations by both L08 and M20 were derived based on LES results.

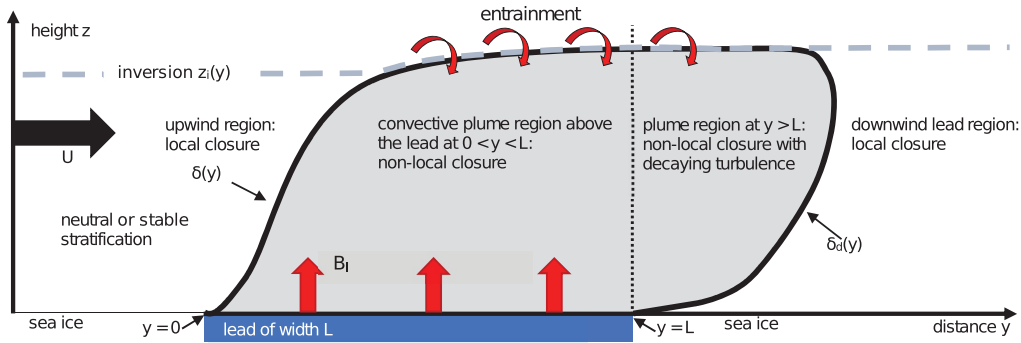


FIGURE 2 Illustration of the non-local closure by M20 to parametrize turbulence in a convective plume with upper and lower boundaries $\delta(y)$ and $\delta_d(y)$, where y is the distance from the upwind lead edge, for an approximately lead-perpendicular flow in an ABL of height z_i on the upwind lead side over a lead of width L surrounded by thick sea ice. U is the upstream ABL-averaged wind speed and B_l the lead-averaged surface buoyancy flux. The principles of the M20 parametrization are explained in the text. Modified from figure 1 of M20

The upper and lower IBL heights $\delta(y)$ and $\delta_d(y)$, which depend on the distance y to the upwind lead edge, act as switching lines. This idea ensures that, even in the downwind region over thick sea ice, turbulence characteristics in the tilted plume depend still on the lead characteristics as, for example, on the mean surface buoyancy flux over the lead B_l . Furthermore, to account for lateral entrainment and dissipation downwind of the lead, an exponentially decaying convection is assumed at $y > L$.

Basically, M20 parametrize the temperature flux $\overline{w'\theta'}$ as

$$\overline{w'\theta'} = -K_h \left(\frac{\partial \bar{\theta}}{\partial z} - \Gamma \right), \quad (5)$$

where Γ is the gradient-independent correction term. K_h is given as

$$K_h = \frac{\kappa u_{*,l} z_p}{\left(\Phi_h - \frac{\kappa z_p}{\theta_{*,l}} \Gamma \right)} \left(\frac{\delta(y) - z}{\delta(y) - z_p} \right)^2 \times \frac{u_{*,l} \kappa z + w_l(y) \delta(y) \{z/\delta(y)\}^{4/3}}{u_{*,l} \kappa z_p + w_l(y) \delta(y) \{z_p/\delta(y)\}^{4/3}}, \quad (6)$$

$z_p \leq z \leq \delta(y)$,

with the lead-averaged friction velocity $u_{*,l}$, the Monin–Obukhov similarity function for heat Φ_h , the lead-averaged scaling value for temperature $\theta_{*,l}$, the convective velocity scale $w_l(y)$, and the height of the upper IBL $\delta(y)$ developing over the lead. Both w_l and δ depend on y . w_l is defined by M20 as

$$w_l(y) = \begin{cases} c(\delta(y)B_l)^{1/3}, & 0 \leq y \leq L \\ c(\delta(y)B_l)^{1/3} \exp\left(-\frac{L-y}{D_w}\right), & y > L, \end{cases} \quad (7)$$

where c is a constant parameter (definition below) and D_w is a decay length-scale for vertical wind fluctuations downwind of the considered lead given by

$$D_w = d_w U \frac{z_i^{2/3}}{B_l^{1/3}}, \quad (8)$$

where d_w is a constant parameter (see below), and B_l is the lead-averaged surface buoyancy flux with

$$B_l = -\frac{g}{\theta_{0,l}} u_{*,l} \theta_{*,l}, \quad (9)$$

where g is the gravitational acceleration and $\theta_{0,l}$ is the lead-averaged surface layer temperature. $\delta(y)$ is obtained after integration of

$$\frac{d\delta}{dy} = \frac{w_e(y)}{U} = \frac{a_e w_{\max}(y)}{U} = \frac{a_e a_m w_l(y)}{U}, \quad (10)$$

using Equation (7), where w_e the entrainment velocity describing vertical entrainment at the plume's upper boundary, w_{\max} is the vertical velocity of the strongest eddies, U is the upstream ABL-averaged wind speed, and a_e and a_m are adjustable parameters (see below). This relation goes back to Monin and Yaglom (1971) and Turner (1986). For $\delta(y)$, this results in

$$\delta(y) = \begin{cases} \min \left\{ z_i, \left(\frac{2a}{3} \frac{B_l^{1/3}}{U} y \right)^{3/2} \right\}, & 0 \leq y \leq L \\ \min \left\{ z_i, \delta_L \left[1 + \frac{D_w}{L} \left\{ 1 - \exp\left(-\frac{L-y}{D_w}\right) \right\} \right]^{3/2} \right\}, & y > L, \end{cases} \quad (11)$$

where the growth of $\delta(y)$ is limited by the height of the capping inversion z_i (set constant by M20 for their cases).

δ_L is defined as

$$\delta_L = \left(\frac{2a B_l^{1/3}}{3 U} L \right)^{3/2}, \quad (12)$$

which guarantees continuity of $\delta(y)$ at $y=L$. The parameter $a = a_e a_m c$ is defined below.

M20 define Γ as in L08, who adjusted an approach by Holtslag and Moeng (1991) to an internal convective ABL so that

$$\Gamma = b \frac{w_l^2(y) \theta_l(y)}{w'^2 \delta(y)}, \quad (13)$$

where b is a constant parameter (see below), θ_l is the convective temperature scale with

$$\theta_l(y) = \begin{cases} -\frac{u_{*,l} \theta_{*,l}}{w_l(y)}, & 0 \leq y \leq L \\ -\frac{u_{*,l} \theta_{*,l}}{w_l(y)} \exp\left(\frac{L-y}{D_\theta}\right), & y > L, \end{cases} \quad (14)$$

where D_θ is a decay length-scale for temperature fluctuations with

$$D_\theta = d_\theta U \frac{z_i^{2/3}}{B_l^{1/3}}, \quad (15)$$

with d_θ as a constant parameter (see below), and where $\overline{w'^2}$ is the vertical velocity variance with

$$\overline{w'^2} = \left[\left\{ 1.6 u_{*,l}^2 \left(1 - \frac{z}{\delta(y)} \right) \right\}^{3/2} + 1.2 w_l^3(y) \frac{z}{\delta(y)} \left(1 - 0.9 \frac{z}{\delta(y)} \right)^{3/2} \right]^{2/3}. \quad (16)$$

As M20, we use a non-local approach also for the eddy diffusivity for momentum inside the plume region:

$$K_m = K_h \left(\frac{\Phi_h|_{z_p} + b \frac{w_l(y) u_{*,l} K z_p}{\Phi_m|_{z_p} \overline{w'^2}|_{z_p} \delta(y)}}{\Phi_m|_{z_p}} \right), \quad \delta_d(y) < z \leq \delta(y), \quad (17)$$

where Φ_m is the Monin–Obukhov similarity function for momentum.

The lower plume boundary $\delta_d(y)$ is defined via a threshold value for the non-local heat flux $F_{\text{crit}} = \rho_0 c_p K_h \Gamma = 0.1 \text{ W} \cdot \text{m}^{-2}$, which is based on LES results as all other above-mentioned unknown parameters. Unless stated otherwise, their values ($c = 1$, $a_m a_e = 1 \pm 0.6$, $a = 1.2$, $b = 2$, $d_w = 1.7$, and $d_\theta = 0.51$) are also used in our simulations. Nevertheless, one of our goals is also to validate these values with the observations from STABLE. For reasons described later, we considered in addition results for

different values of a for two of the observed lead cases (Section 5).

3.2 | Model set-up

An overview of all model runs is shown in Table 1, where we use abbreviations to denote the case and the applied parametrization (e.g., 1003-MIX denotes the model run for 10 March performed with the local closure and 2503-NL1 denotes a model run for 25 March with the non-local closure). We basically distinguish the surfaces of thick sea ice and leads only by differences in the surface roughness lengths z_0 and surface temperatures. As in L08 and M20, $z_0 = 10^{-3} \text{ m}$ is prescribed for thick sea ice and $z_0 = 10^{-4} \text{ m}$ for lead surfaces. The ratio between the surface roughness lengths for momentum and temperature (z_0/z_t) is assumed as 10. For reasons described later, we performed one model run with $z_{0,l}/z_{t,l} = 100$ (Table 1), where the subscript l refers to the lead surface. Unfortunately, these roughness lengths cannot be evaluated with observations from STABLE since the flight legs were not arranged specifically to derive the required near-surface neutral transfer coefficients.

Regarding the surface humidity, we assume saturation over ice. The surface temperatures (Table 2) derived from the observations (Figure 1a,b,c) are kept constant in time. For 25 and 26 March, $T_{s,l}$ is set constant all over the leads since the observed variability was small (Section 2). For 10 March, we consider the observed fetch-dependence of $T_{s,l}$. Nevertheless, for that case also, we apply lead-averaged values for the parameters $\theta_{*,l}$ and B_l in the non-local closure so that the integration of Equation (10) is not violated by the fetch-dependence of $T_{s,l}$.

Inflow profiles are generated with the 1D model version of METRAS based on measurements at the upwind side of the leads. Both wind speed and direction are obtained at the inflow boundary with height-independent, observation-based values of the geostrophic wind components u_g and v_g . Both observed and modelled inflow profiles are shown in Figure 3.

On 10 March, higher ABL temperatures were measured at $y \approx -7 \text{ km}$ distance to the upwind lead edge than above the lead (Section 2.1 and Figure 3a). Moreover, the upwind ABL-averaged wind speed is slightly overestimated when compared to the measurements above the lead (Figure 3d). Hence, to ensure comparability, we assume that, at the inflow position, the prescribed air temperature matches the sea ice surface temperature in the lowest levels. This explains the deviation between the observed and modelled temperature profiles, which is larger than in the other two cases. We could also not obtain the observed increase of wind speed above z_i

TABLE 1 Overview of the settings for the numerical simulations

Model run	Closure scheme	Method to calculate $z_i(y)$	Value for a	Further specifications
1003-MIX	local	fixed value, $z_i(y) = 95$ m	—	—
1003-NL1	non-local	fixed value, $z_i(y) = 95$ m	1.2	—
1003-NL2	non-local	contour; threshold: $\theta _c = 246.8$ K	1.2	—
1003-NL3	non-local	contour; threshold: $\theta _c = 246.8$ K	1.2	$z_{t,l} = 0.01z_{0,l}$
2503-MIX	local	fixed, $z_i(y) = 90$ m	—	—
2503-NL1	non-local	fixed, $z_i(y) = 90$ m	1.2	—
2503-NL2	non-local	fixed, $z_i(y) = 90$ m	0.75	—
2503-NL3	non-local	contour; threshold: $\theta _c = 247.4$ K	0.75	—
2603-MIX	local	fixed, $z_i(y) = 190$ m	—	—
2603-NL1	non-local	fixed, $z_i(y) = 190$ m	1.2	—
2603-NL2	non-local	contour; threshold: $\theta _c = 247.2$ K	0.9	—

Note: The closure schemes refer to the local mixing-length closure (MIX) and the non-local closure (NL) of M20 (Section 3.1). $z_i(y)$ is the ABL height in the model, for which the upwind observed value is prescribed in some runs, while in some other runs a y -dependent ABL height is used, with y as the distance from the lead edge (Section 5.1). Values in the fourth column refer to the parameter a in the non-local closure of M20 (Sections 3.1 and 5.2 give further details). $z_{t,l}$ and $z_{0,l}$ are heat and momentum roughness lengths for lead surfaces (Sections 3.2 and 5.3.)

TABLE 2 Initial conditions for model runs of the discussed case-studies from STABLE

Parameter	Dates for model runs		
	10 March 2013	25 March 2013	26 March 2013
L (km)	2.3	2.1	1.6
$T_{s,i}$ ($^{\circ}\text{C}$)	-25.6	-25.5	-25.1
$T_{s,l}(y)$ ($^{\circ}\text{C}$)	$\left\{ \begin{array}{ll} -12.0 & \text{for } 0.0 \leq y \leq 0.8 \text{ km} \\ -3.0 & \text{for } 0.8 < y \leq 1.2 \text{ km} \\ -12.0 & \text{for } 1.2 < y \leq 1.5 \text{ km} \\ -4.0 & \text{for } 1.5 < y \leq 1.8 \text{ km} \\ -13.0 & \text{for } 1.8 < y \leq 2.3 \text{ km} \end{array} \right.$		
$\overline{\partial\theta/\partial z}$ ($\text{K}\cdot\text{m}^{-1}$)	0.0	0.014	0.003
z_i (m)	95	90	190
u_g ($\text{m}\cdot\text{s}^{-1}$)	-0.9	-0.6	-3.6
v_g ($\text{m}\cdot\text{s}^{-1}$)	-4.0	-8.4	-6.9
p_0 (hPa)	1028	1034	1029

Note: L is the lead width, $T_{s,i}$ and $T_{s,l}(y)$ are the surface temperatures prescribed for sea ice and lead surfaces, respectively, where y is the distance to the upwind lead edge. $\overline{\partial\theta/\partial z}$ is the average upwind vertical potential temperature gradient below the bottom of the capping inversion at height z_i as observed upwind of the lead. u_g and v_g are the lead-parallel and lead-orthogonal height-independent geostrophic wind components, and p_0 is the observed surface pressure.

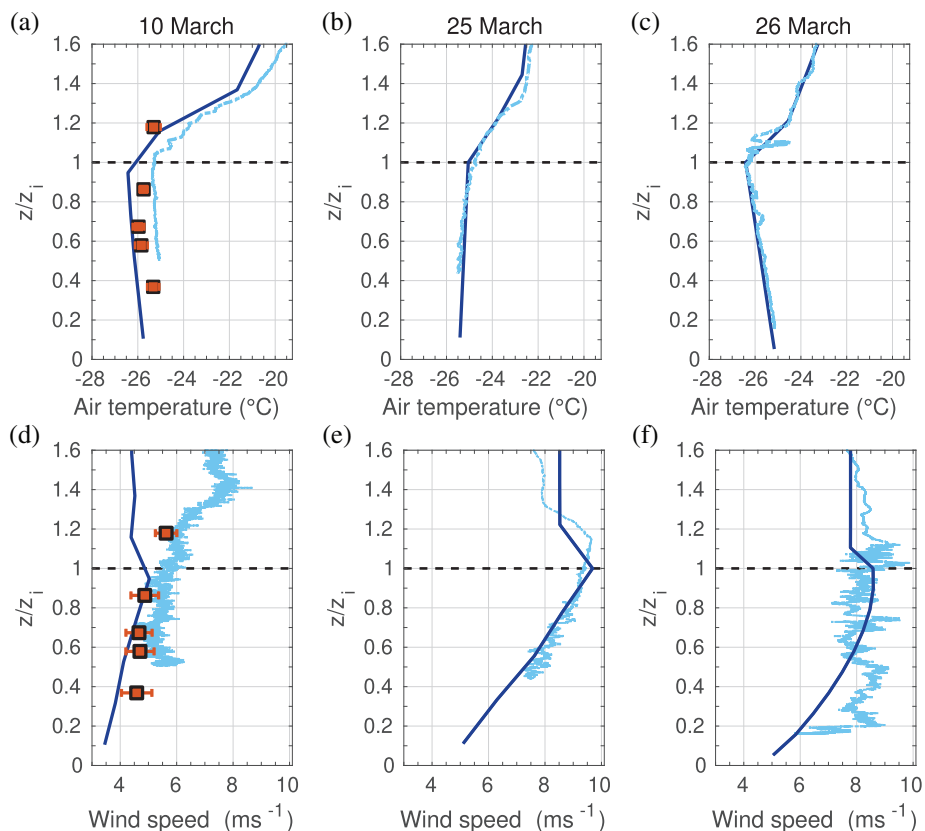
and prescribed the geostrophic wind to a smaller value to ensure matching with the ABL wind above the lead (squares in Figure 3d).

For the other two cases, observed and modelled inflow profiles differ only marginally (Figure 3b,c,e,f). For 25 March, only the observed and modelled vertical locations of the wind speed maximum differ slightly (Figure 3e).

For 26 March, the 1D model underestimates the observed inflow wind speed between $0.2z_i$ and $0.5z_i$ (Figure 3f), but agrees well with the observation outside of this range.

Further initial values for the model runs are shown in Table 2. After the initialisation, the model equations are integrated until quasi-stationary conditions are reached

FIGURE 3 Profiles observed near the upstream edges of the three leads (light solid lines) and the corresponding simulated inflow profiles (dark solid lines) of (a–c) atmospheric temperature and (d–f) wind speed plotted as functions of the non-dimensional height z/z_i , where z_i is the upwind observed ABL height. (a, d) are for 10 March 2013, where $z_i = 95$ m and the upwind measured profiles were obtained at $y = -7$ km distance. Profiles measured above the lead at $y = 1.3$ km are also shown (squares with error bars). (b, e) are for 25 March 2013 with $z_i = 90$ m. Measured profiles were obtained at $y = -2$ km. (c, f) are for 26 March 2013 with $z_i = 190$ m. Measured profiles were obtained at $y = -1.5$ km



(approximately after 2 hr integration time). Simulation results are then compared to the ABL observations obtained by aircraft above and downstream of the respective leads.

4 | SIMULATION RESULTS WITH NON-MODIFIED PARAMETRIZATIONS

We analyse three basic features. First, turbulent fluxes and ABL structures of temperature and wind are examined based on vertical cross-sections in the lead-perpendicular direction. Second, vertical structures at individual positions obtained from profiles of both mean quantities and turbulent fluxes are analysed. Third, we discuss the development of variables at a constant height level as a function of distance.

For each case described in the following subsections, all cross-sections are shown using the non-dimensional height z/z_i , where z_i is the upwind observed ABL height (Section 2 gives the respective values). For figures showing vertical profiles, all observations are shown as values averaged over the respective lead-parallel flight legs with error bars denoting the statistical error (Section 2). The potential temperature data including their error bars are based on T15 (their figures 5a, 14a, and 17a). As T15, for

the calculation of the turbulent fluxes, we also applied a band-pass filter on measurements of both wind components and potential temperature with cut-off frequencies of 0.1 and 50 Hz, but unlike T15, we slightly modified some legs to reduce inhomogeneity and use a band-pass filter (MATLAB version 2020a) reducing artificial noise at the beginning of the legs. Thus, some of our flux values slightly differ from those in T15. Moreover, we consider the absolute value of the vertical flux of horizontal momentum, $|\tau|$, with $\tau = -\bar{\rho}(\tau_{13}, \tau_{23}) = -\bar{\rho}(\overline{u'w'}, \overline{v'w'})$. For 10 March, this is contrary to T15, who considered only the x -component τ_{13} . As a new feature, we considered also vertical profiles of the horizontal wind speed.

All simulated vertical profiles are shown as solid, coloured lines with a shaded region around. The lines refer to results at a certain distance from the upwind lead edge, which agrees with the position of the corresponding measurements averaged over the respective lead-parallel flight leg. The shaded region is added to include model results of ± 300 m upwind and downwind of every position to account for remaining uncertainty of the fetch lengths (although corrected by filtering), for example, by the slight differences between the modelled and observed wind directions. Thus, we can also examine whether at least the modelled and observed patterns agree except for a potential horizontal shift of the structures.

4.1 | Model runs 1003-MIX and 1003-NL1

Simulated vertical cross-sections of the model runs 1003-MIX and 1003-NL1 are shown in Figure 4. Some general features can be clearly identified, which are also shown for the other two cases discussed below. First, an inclined plume developing over the lead is obvious from the heat flux patterns of both runs (Figure 4a,b), where the simulated plume shapes differ depending on the applied parametrization. While in run 1003-MIX positive heat fluxes extend far into the lead's downwind region, a clear downwind plume boundary is simulated by run 1003-NL1 with negative fluxes further downstream starting at $y \approx 3$ km. In run 1003-NL1, entrainment fluxes are simulated near z_i above the lead at $y \approx 0.8$ km, which indicates that the plume reaches the inversion layer at that distance. Second, the developing plume leads to an ABL warming and also affects ABL stratification as shown in the patterns of the potential temperature (Figures 4c and 4d). While the application of the local closure causes a slightly unstable stratification in almost the whole downwind mixed layer (denoted in Figure 4c), a slightly stable stratification is obtained with the non-local closure (denoted in Figure 4d). This causes a fundamental difference in the heat fluxes, which are directed upward/downward in this region when the local/non-local closure is applied. Note that a stabilisation of the downwind ABL was also obtained by M20 in their LES of idealised cases at near-neutral upwind stratification.

Modelled horizontal wind speed patterns differ only very slightly from each other (Figures 4e,f). In both simulations, a pronounced wind speed maximum is indicated near z_i , where it is more or less destroyed further downwind by enhanced vertical mixing due to the lead-generated convection.

In the pattern of the momentum flux, a clear maximum is obtained with both closure schemes above the lead (Figure 4g,h). In run 1003-MIX, the maximum is slightly more pronounced and it occurs a few hundred metres further downwind than in run 1003-NL1.

Simulated and observed profiles for 10 March are shown in Figure 5. The general observed structure of the heat flux profiles is basically represented by both model runs (Figures 5a,b). At $y = 1.3$ km (near the lead's centre), surface heat fluxes of 110 to 195 $\text{W}\cdot\text{m}^{-2}$ are simulated, where the large range of model results reflects the uncertainty as described above (Sections 2, 3.2, and 4). Above the surface layer, the observed almost linear decrease of heat fluxes is well represented with both model runs. Near the downwind lead edge at $y = 2.3$ km, the observed structure of an elevated heat flux maximum in the ABL centre is also reproduced. However, the simulated heat fluxes exceed the observed values. This is obvious especially over

the lead's centre, while at the downwind lead edge the measurements are at least in the scatter of the modelled values (shaded region) obtained with the non-local closure (Figure 5b). Thus, one possible explanation of the overestimation is the uncertainty in the fetch and in the exact position of the aircraft relative to the slightly curved lead edge.

Although the simulated heat fluxes exceed the observed values above the lead, the simulated temperature profiles agree well with the observations at $y = 1.3$ km (Figure 5c,d). Near $y = 2.3$ km, the simulated values are slightly below the mean observed temperatures, especially for the observed value near $0.9z_i$. This is especially obvious for the run 1003-MIX, where an unstable stratification is obtained. Following the run 1003-NL1, rather a neutral or slightly stable stratification is shown, which better resembles the observations. The slight underestimation of observed temperatures might be explained by an under-represented vertical entrainment of heat through the capping inversion.

The observed wind profiles are only partially well represented by the model runs (Figure 5e,f). Above the lead at $y = 1.3$ km, measured and simulated profiles agree well below z_i , but the observed increase in wind speed above z_i does not match with the modelled one, which is due to the mismatch in the inflow profile (Figure 3d). Near the lead's downwind edge at $y = 2.3$ km, the simulated values exceed the observations by approximately $1 \text{ m}\cdot\text{s}^{-1}$ in the entire ABL. For the observed momentum fluxes at $y = 2.3$ km, a strong underestimation is obtained by both model runs (Figure 5g,h). At $y = 1.3$ km, the momentum fluxes modelled by both runs agree better with the observed ones, especially the simulation results of run 1003-NL1 which almost perfectly hit the observed values.

4.2 | Model runs 2503-MIX and 2503-NL1

For 25 March, the differences between the model runs MIX and NL1 (Figure 6) are not as pronounced as for 10 March. The most important differences concern both structure and vertical extent of the plumes, which is most obvious in the heat fluxes (Figure 6a,b). In run 2503-NL1, an abrupt increase of the upper plume boundary is obtained over the second half of the lead, unlike in run 2503-MIX.

The temperature patterns obtained by both model runs for 25 March differ strongly from those for 10 March, indicating stable stratification on the upwind and downwind side of the lead (Figures 6c,d). Compared to METRAS simulations of 10 March and of the idealised cases considered by M20, the formation of a stable stratification downwind of the lead is a new feature, when the local

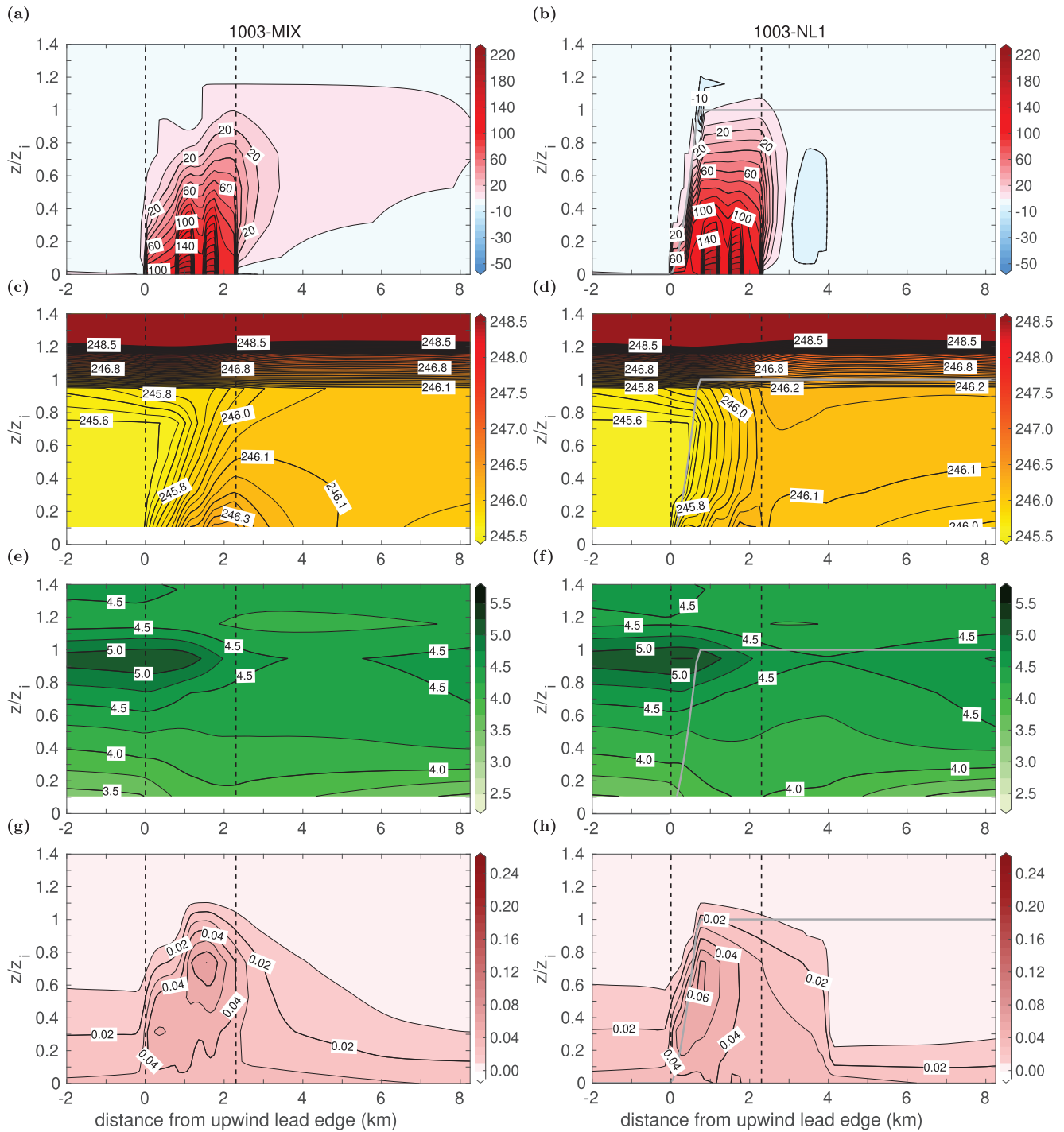


FIGURE 4 Vertical cross-sections obtained with METRAS for 10 March 2013 (runs 1003-MIX and 1003-NL1; Table 1) plotted against the non-dimensional height z/z_i , where $z_i = 95$ m is the upwind observed ABL height. (a, b) show the sensible heat flux in $\text{W}\cdot\text{m}^{-2}$ (with positive contour interval $10 \text{ W}\cdot\text{m}^{-2}$ and negative interval $5 \text{ W}\cdot\text{m}^{-2}$), (c, d) the potential temperature in K, (e, f) the horizontal wind speed in $\text{m}\cdot\text{s}^{-1}$, and (g, h) the momentum flux in $\text{N}\cdot\text{m}^{-2}$. The lead is between the vertical dashed black lines. In (b, d, f, h), the solid grey lines show the upper IBL height according to Equation (11)

closure is used. It is clearly related to the stable stratification already upwind of the lead. For 2503-NL1, also the counter-gradient flux contributes to the ABL stabilisation downwind of the lead (see also Section 6) and the simulated downwind stability is slightly stronger than with

2503-MIX. The observed influence of the plume on the temperature structure in the capping inversion (Figure 1d) is not represented, neither by 2503-MIX nor by 2503-NL1.

The wind speed maximum at the upstream side and its destruction by the plume over the lead are reproduced by

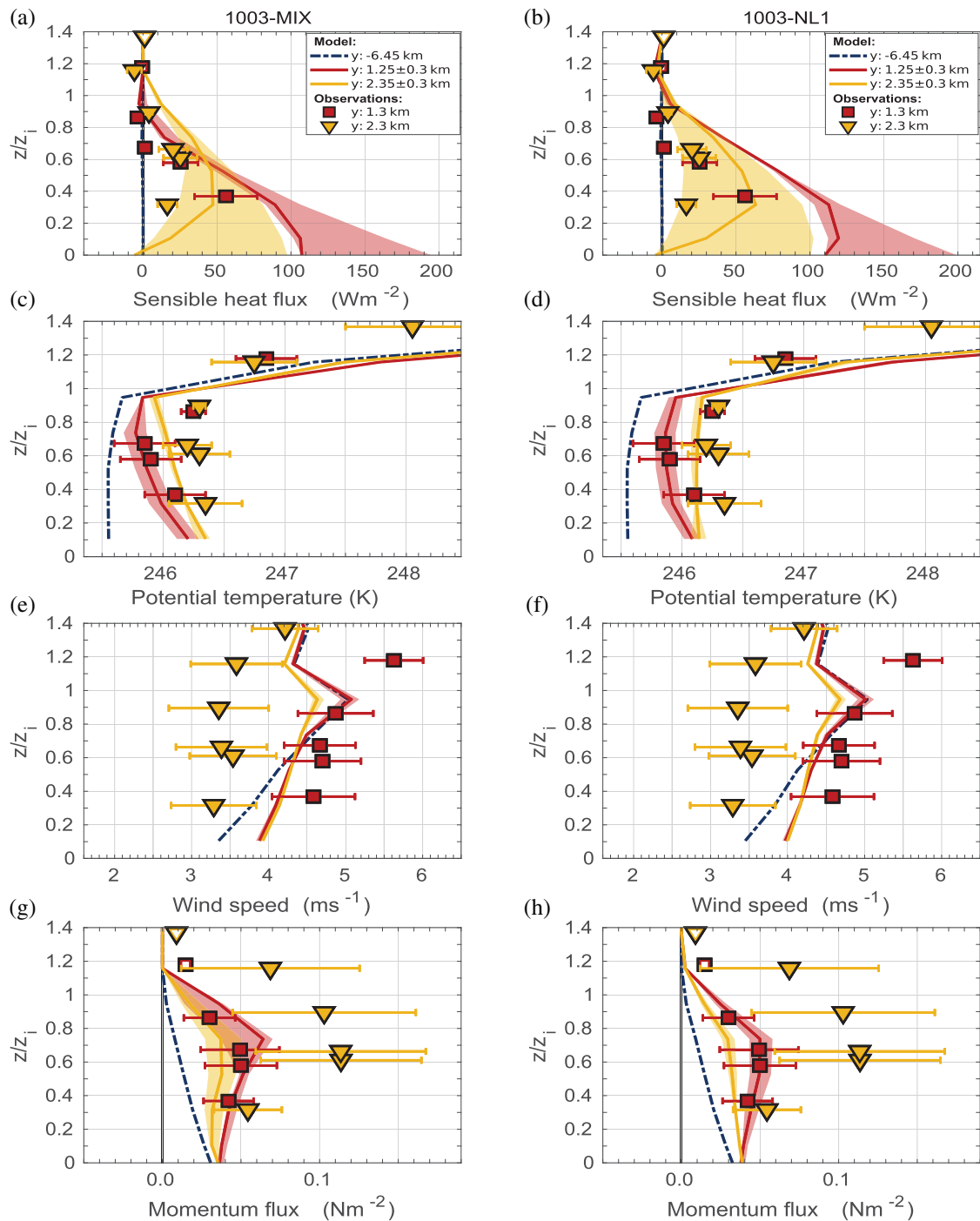


FIGURE 5 Vertical profiles from simulation results obtained with METRAS (coloured lines and shaded regions, runs 1003-MIX and 1003-NL1; Table 1) and the corresponding observations with measurement uncertainties (points with error bars, partly from T15) for 10 March 2013 at different locations y , where y is the distance from the upstream lead edge, plotted against the non-dimensional height z/z_i , where $z_i = 95$ m is the upwind observed ABL height. (a, b) show the sensible heat flux in $\text{W}\cdot\text{m}^{-2}$, (c, d) the potential temperature in K, (e, f) the wind speed in $\text{m}\cdot\text{s}^{-1}$, and (g, h) the momentum flux in $\text{N}\cdot\text{m}^{-2}$. The lead is located between $y = 0$ km and $y = 2.3$ km. Open symbols mark values obtained from legs with observed intermittent turbulence (T15)

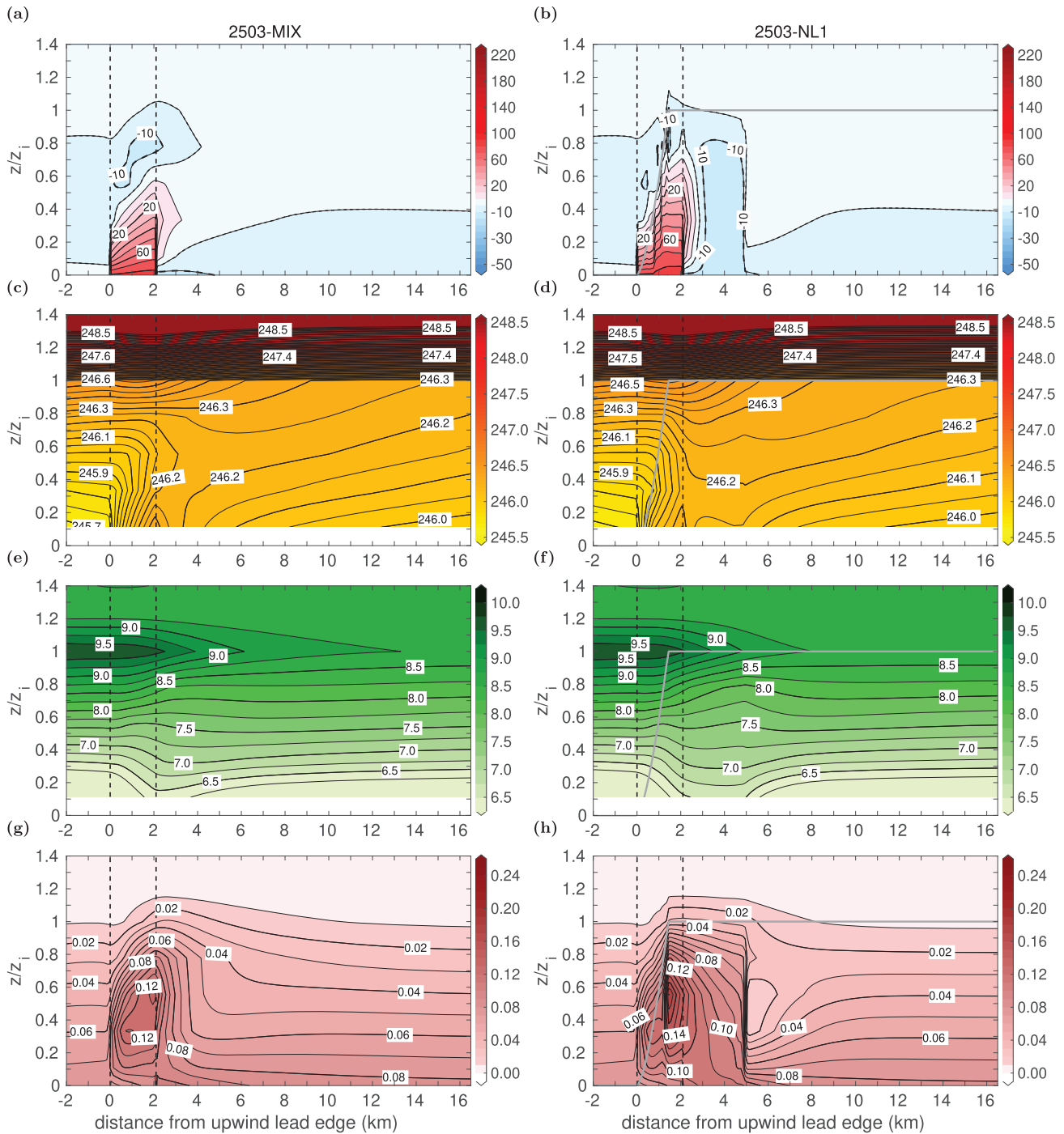


FIGURE 6 As Figure 4, but for the model runs 2503-MIX and 2503-NL1 (Table 1) for 25 March 2013. The upwind observed ABL height is $z_i = 90$ m

the model, slightly better by 2503-NL1 than by 2503-MIX (Figure 6e,f). However, the observed recovering wind maximum further downwind is not captured, irrespective of the closure.

Regarding the momentum fluxes, slightly higher values are obtained with 2503-NL1 than with 2503-MIX (Figure 6g,h). Moreover, the region with increased momentum fluxes depicting the convective plume extends

further downwind and reaches higher altitudes in run 2503-NL1.

A comparison between the simulated heat flux profiles of both model runs and the observations on 25 March (Figure 7a,b) points, in general, to a better representation of the observed heat fluxes below z_i than on 10 March. Moreover, heat fluxes obtained with the non-local closure (2503-NL1) vary more strongly with distance than those

obtained with the local closure (2503-MIX) indicated by the wider shaded areas around the profiles at single locations. This implies a seemingly larger impact of the fetch when the non-local closure is used. Two major differences between simulated and observed heat fluxes are obvious. First, near $0.7z_i$, the minima with negative heat fluxes are less pronounced in both simulations than in the observations. Second, the minimum near z_i observed downwind of the lead at $y = 2.7$ km is almost absent in the simulations.

For the temperature above the lead's centre ($y = 1.3$ km), almost the same profiles are obtained by both runs in good agreement with the corresponding measurements at the lowermost flight level at $0.4z_i$, but between $0.4z_i$ and $0.7z_i$ both runs underestimate the observed stability (Figure 7c,d). The downwind observed ABL warming effect is also underestimated by both runs, where the temperature profile at $y = 2.7$ km simulated by 2503-NL1 agrees slightly better with the observations than by 2503-MIX. There is also an important difference between the results obtained with both closures that concerns the direction of fluxes. Near $y = 2.7$ km, the observed ABL temperature increases with height between $0.4z_i$ and $0.7z_i$, which is indicative of counter-gradient heat transport in that layer (see also Section 6). This temperature increase is reproduced in the result with the non-local closure, but it cannot be captured by the local closure, where the temperature slightly decreases with height at the same location.

The observed wind profiles at all three locations are fairly well reproduced by the model (Figure 7e,f). Simulated momentum fluxes are basically smaller than the observed ones (Figure 7g,h), especially in run 2503-MIX. In run 2503-NL1, there is a slightly better representation of the observed values, especially in the lead's downwind region near $y = 4.3$ km.

4.3 | Model runs 2603-MIX and 2603-NL1

As for the previous two cases, also for 26 March, the differences between the two model runs (2603-MIX and 2603-NL1) concern the plume's vertical extent and inclination (Figure 8). A less inclined plume is obtained by run 2603-MIX due to a stronger plume growth above the first half of the lead than by run 2603-NL1. Thus, in 2603-MIX, the upper plume boundary at $y = L$ is at $0.7z_i$ (Figure 8a) and reaches the inversion layer far downwind of the lead at 6 km distance, while in 2603-NL1, z_i is reached already at $y = L$ (Figure 8b).

The temperature distribution downwind of the lead shows an almost neutral layer with 2603-MIX (Figure 8c) and a slightly stable layer with 2603-NL1 (Figure 8d). In the simulated wind speed patterns (Figure 8e,f), only

marginal differences appear between the two model runs. The general structure is similar to the previously discussed cases. Differences in the momentum fluxes occur mainly in the region $y > 6$ km (Figure 8g,h).

Compared to the measured vertical profiles (Figure 9), run 2603-MIX strongly overestimates the heat fluxes above the lead's centre (at $y = 0.7$ km), whereas at the lead's downwind edge (at $y \approx 1.5$ km), the observed flux profile is well represented (Figure 9a), but with an underestimation of the flux at the lowermost level. Further downwind, the simulated heat fluxes are much smaller than the observed ones, but at least the structure of an elevated flux maximum is basically represented. The corresponding results obtained by run 2603-NL1 show the opposite (Figure 9b) with very well reproduced fluxes over the lead centre, but overestimated fluxes in the upper half of the ABL near the lead's downwind edge. As in 2603-MIX, large deviations from the observations are also obvious near $y = 3.0$ km and $y = 4.3$ km. Thus, the plume's horizontal extent is underestimated by both runs.

The observed temperature profiles are slightly better represented by the simulation using the non-local closure. This concerns especially the slightly stable stratification at 4.3 km distance (Figure 9c,d), which is reproduced only by run 2603-NL1.

As for 25 March, the observed wind profiles are well reproduced by both model runs also for 26 March (Figure 9e,f) and also elevated momentum flux maxima are simulated in both runs, where their vertical location increases with increasing y (Figure 9g,h). At $y = 0.7$ km, the momentum fluxes simulated by both runs slightly exceed the observed values. Downwind of the lead, 2603-NL1 slightly better resembles the observed flux patterns than 2603-MIX, but the modelled fluxes are basically smaller than the observed ones.

5 | MODIFICATION OF THE M20 PARAMETRIZATION

The simulation results in Section 4 showed that the general structure of the ABL is fairly represented by model simulations using the local or the non-local closure. Furthermore, there is no clear difference in the results obtained with the two closure types as in the idealised cases discussed in M20 with neutral stratification upwind of the lead. The non-local closure shows slight advantages in some aspects. For example, the downwind temperature profiles and momentum fluxes on 25 March obtained with the M20 closure agree slightly better with the observations than those obtained with the local closure. However, in some other aspects the local closure shows advantages. The results obtained with the M20 closure also revealed

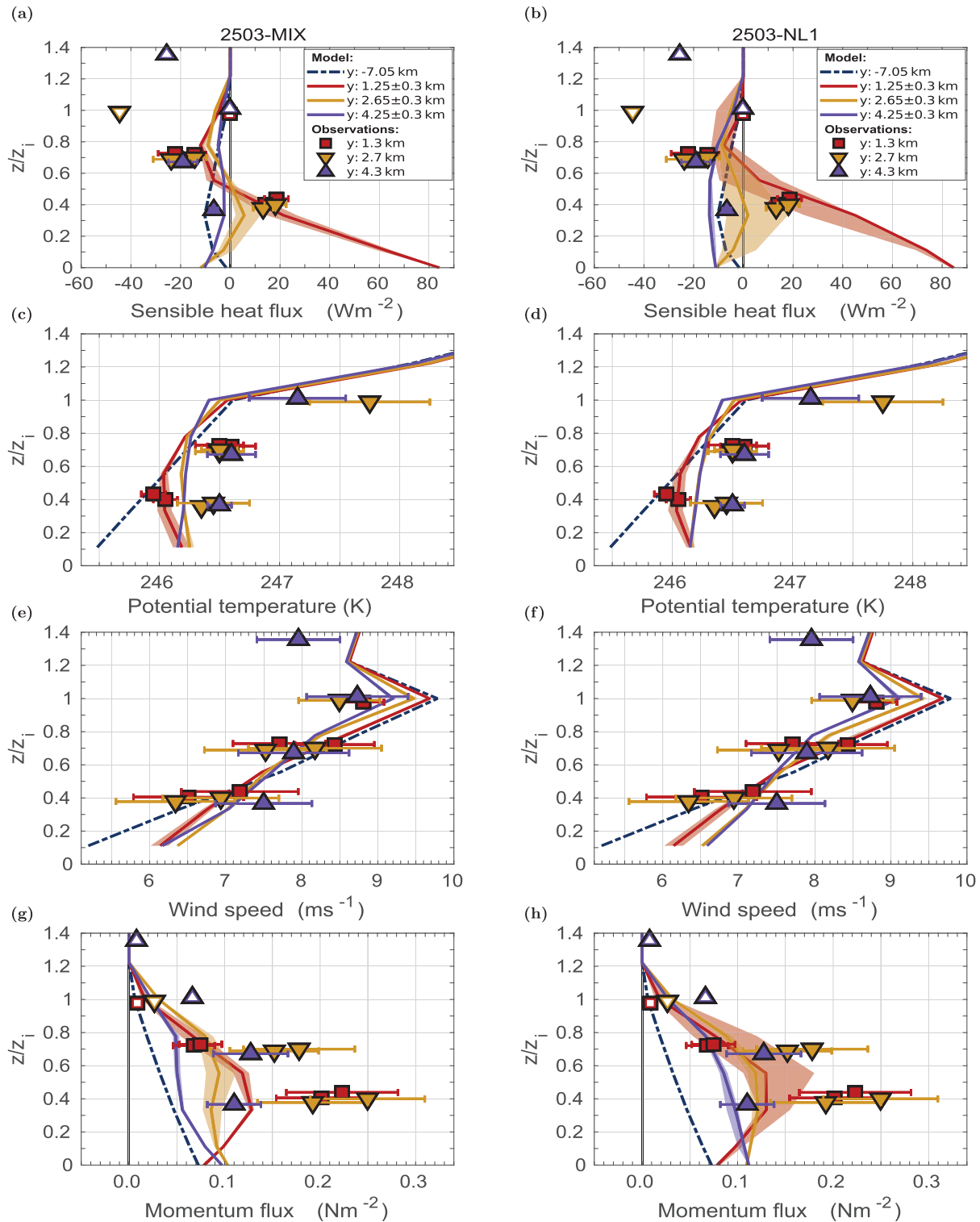


FIGURE 7 As Figure 5, but for model results of runs 2503-MIX and 2503-NL1 (Table 1) and observations for 25 March 2013. The upwind observed ABL height is $z_i = 90$ m. The lead is located between $y = 0$ km and $y = 2.1$ km

two main drawbacks when compared to the measurements. The first concerns the underestimation of the observed ABL warming effect downwind of the leads shown for all three cases. We speculate that this is most probably due to underestimated vertical entrainment.

Second, for 25 and 26 March, the plumes simulated by the runs 2503-NL1 and 2603-NL1 grew too quickly compared to the observations. Most probably, this is due to the stable stratification upwind of the leads that might cause the lead-generated plume to grow more slowly than for neutral

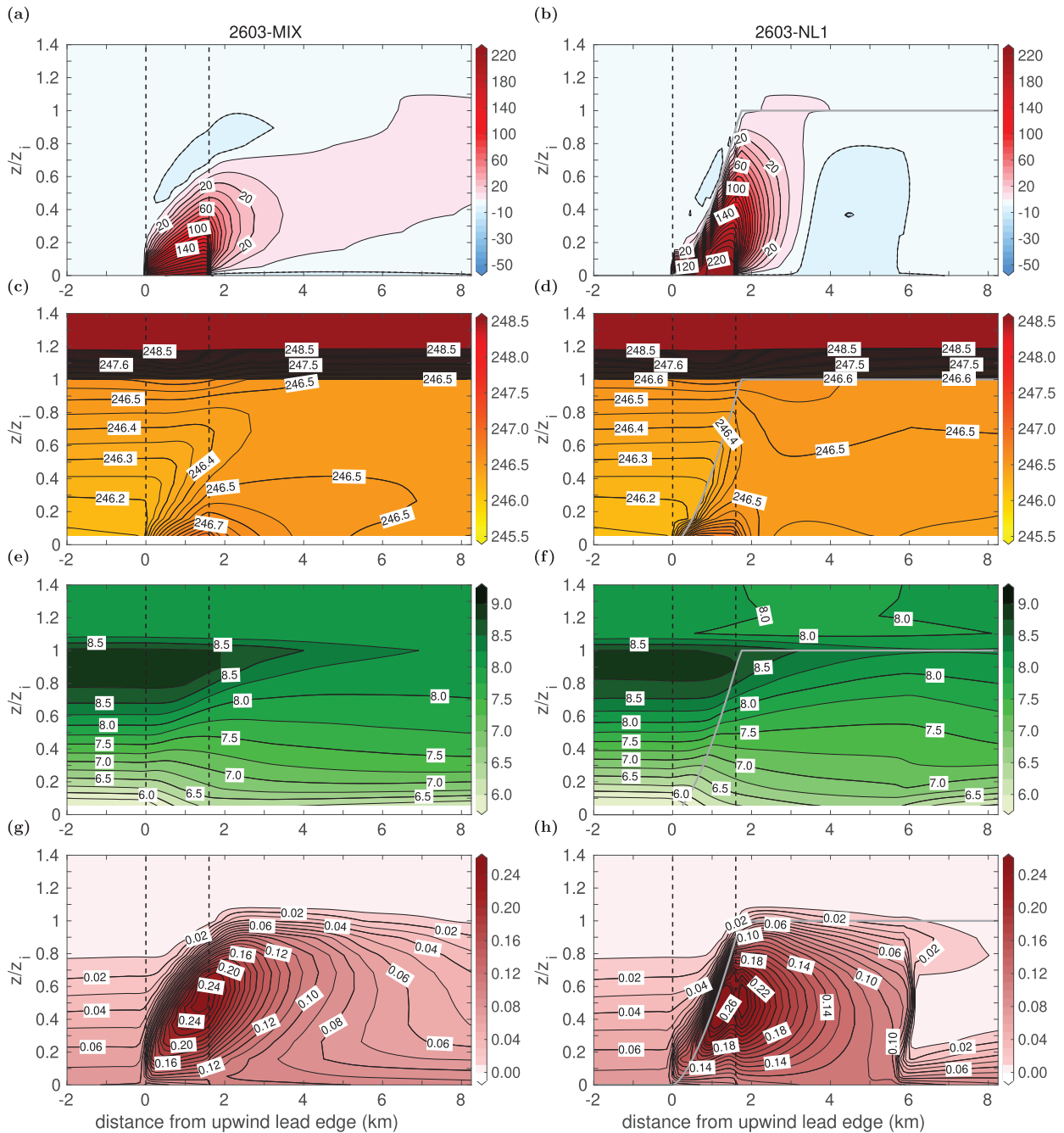


FIGURE 8 As Figure 4, but for the model runs 2603-MIX and 2603-NL1 (Table 1) for 26 March 2013. The upwind observed ABL height is $z_i = 190$ m

stratification (T15). This behaviour could not be captured by the closure developed so far for neutral inflow. Hence, in the following, we present two further modifications of the M20 closure to overcome these drawbacks.

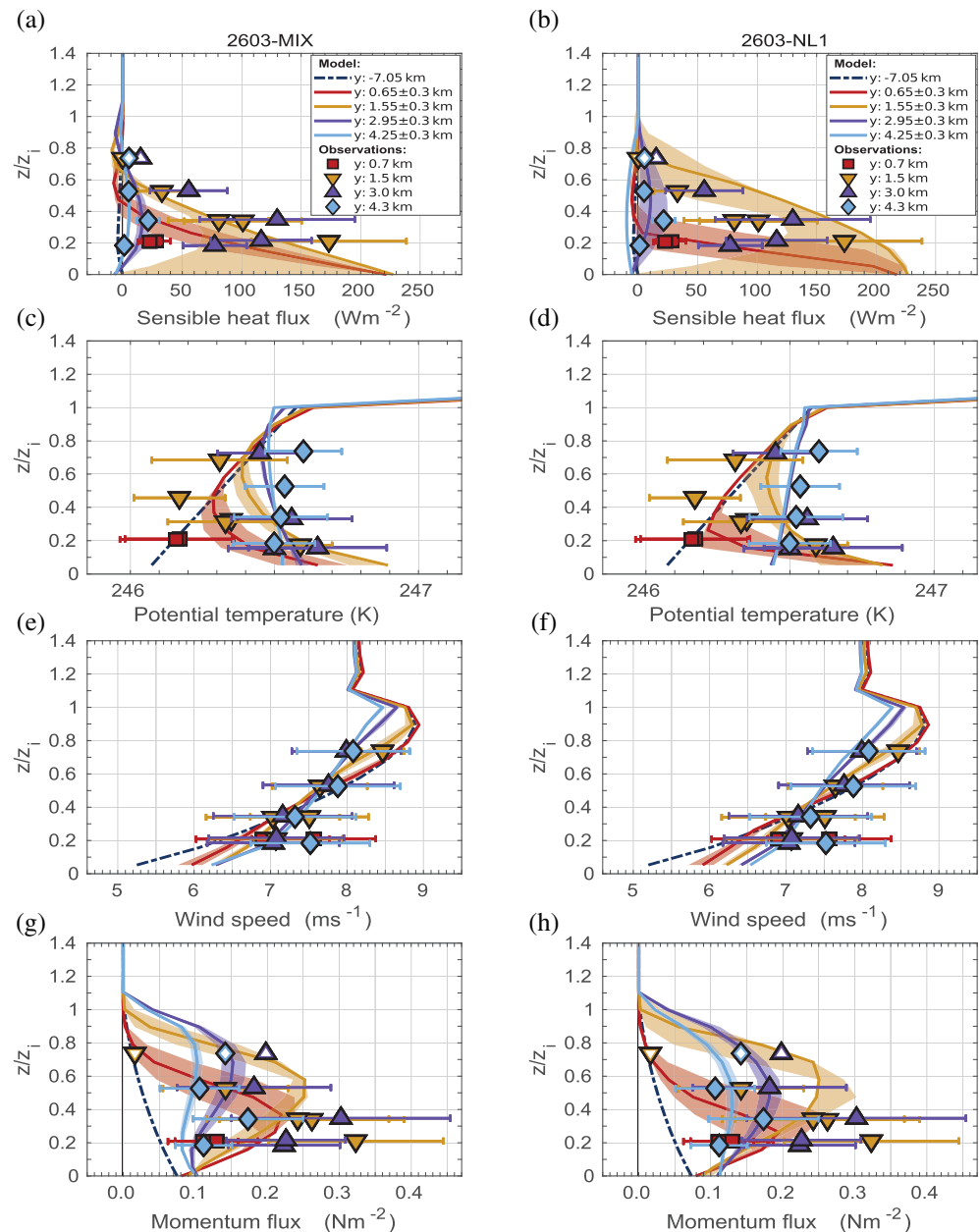
5.1 | Determination of the ABL height z_i

The observations by T15 revealed that the convection over leads can be strong enough to penetrate into the capping

inversion, which leads to vertical entrainment fluxes so that z_i increases with distance. Such effects were clearly observed during STABLE, where the measured z_i upwind of the lead differed clearly from the value downwind of the lead (Section 2). To include the penetration effect, we consider modifications for the parameter z_i in the M20 parametrization.

We introduce a diagnostic determination of a y -dependent inversion height, $z_i(y)$, following the methods of Sullivan *et al.* (1998). They investigated the temporal

FIGURE 9 As Figure 5, but for model results of runs 2603-MIX and 2603-NL1 (Table 1) and observations for 26 March 2013. The upwind observed ABL height is $z_i = 190$ m. The lead is located between $y = 0$ km and $y = 1.6$ km



evolution of a surface-heated, initially neutrally stratified convective ABL, with a finite potential temperature jump across the inversion followed by a uniform lapse rate above, which includes the evolution of the ABL height z_i . They used a 3D LES model with a nested grid in the inversion layer and analysed three different methods – the flux method, contour method and gradient method (Sullivan *et al.*, 1998). These methods are used to determine z_i at every horizontal grid point position (here at each y). Following the flux method, z_i is defined as the vertical location of the minimum heat flux. Following the contour method, z_i is defined as the vertical location of a specific contour line of the potential temperature, for which a specific value θ_c has to be prescribed. The selected potential temperature contour is then tracked

along distance y and its respective vertical position is set equal to z_i . Following the gradient method, z_i is defined as the vertical location of the maximum vertical potential temperature gradient. Sullivan *et al.* (1998) also showed that z_i obtained via the flux method is, in general, lower than with the other methods, which corresponds with results of laboratory investigations by Deardorff *et al.* (1980). Furthermore, Sullivan *et al.* (1998) found that the flux method underestimated both z_i and turbulence in the inversion.

We performed simulations applying all three methods for the $z_i(y)$ determination. The implementation of the y -dependent z_i in the model was done as follows. First, at each numerical time step, the variables needed to determine $z_i(y)$ are vertically linearly interpolated from the

numerical grid with 20 m vertical spacing to a 5 m spacing. This concerns the potential temperature for all three methods as well as K_h and Γ for the flux method. Second, based on those interpolated fields, $z_i(y)$ is calculated at each grid point in the lead-perpendicular direction using the respective method. Third, the final values for $z_i(y)$ are obtained after applying a running mean over five points in the lead-perpendicular direction to smooth spatial oscillations of $z_i(y)$. The values finally obtained for $z_i(y)$ as a function of distance then mark the (fetch-dependent) upper limit for the upper IBL height $\delta(y)$ (Equation (11)). Moreover, we assume that variations in $z_i(y)$ for $y > y_{z_i}$, where y_{z_i} marks the distance where the upper plume boundary intersects with the upwind value of z_i , are only due to the influence of the plume in the inversion layer. For the flux method, we calculate $z_i(y)$ based on the heat flux profile at time step $t - 1$ because z_i itself is needed to calculate the heat flux, and we set the observed upstream ABL height as a minimum value for $z_i(y)$. This is because, downwind of the lead, the location of the minimum vertical heat flux is likely to be near the ice surface in the devolving near-surface stable IBL (not shown). For θ_c used in the contour method, we prescribe the temperature values 10 m above $z_i(y)$ at the inflow boundary.

For 10 March, the results for $\delta(y)$ with the fetch-dependent upper limit $z_i(y)$ are shown in Figure 10 dependent on the method used for determining $z_i(y)$. Note that the small-scale variation in $z_i(y)$, especially for the gradient method, is due to linear interpolation, so for numerical rather than for physical reasons. Following the flux method, $z_i(y)$ remains constant at its upwind level of 95 m until $y = 4$ km and then it strongly increases to about 120 m until $y = 7.5$ km. Thus, the increase in $z_i(y)$ occurs much farther downwind than in the observations (Section 2.1). Moreover, $z_i(y)$ increases downwind of the

convective plume region for the first time, so downwind of $\delta_d(y)$. Thus, no improvements can be expected by this method for the non-local closure.

Following the gradient method, $\delta(y)$ strongly increases to about 120 m already above the lead's centre and it remains almost constant with increasing y (Figure 10). Thus, much higher values than the observed downwind value are obtained for $z_i(y)$ already above the lead causing overestimated entrainment (not shown).

Following the contour method (here with $\theta_c = 246.8$ K), a monotonic increase of $\delta(y)$ is obtained above the lead starting at $y \approx 0.8$ km. Further downwind, $z_i(y)$ remains constant at 115 m, which is higher than the observed value of 101 m (Section 2.1). Nevertheless, $z_i(y)$ as obtained with this method seems to be the best representation of a continuously rising ABL height with distance y . Hence, we consider additional simulations only with the contour method for all cases (see below).

5.2 | Adjustment of parameter a to stably stratified inflow conditions

For the parameter a , which denotes the simulated plume inclination, M20 obtained the value 1.2 based on their LES results of idealised cases with upwind neutral stratification. However, in a stable environment, it can be expected that a lead-generated plume penetrates into the ABL more slowly than in neutral conditions (T15). This is supported by the findings of T15, who compared the observed IBL height on 25 March with the corresponding parametrization by L08, which forms the basis for the M20 approach and which is also designed for a near-neutral inflow. T15 found that the L08 parametrization using the original

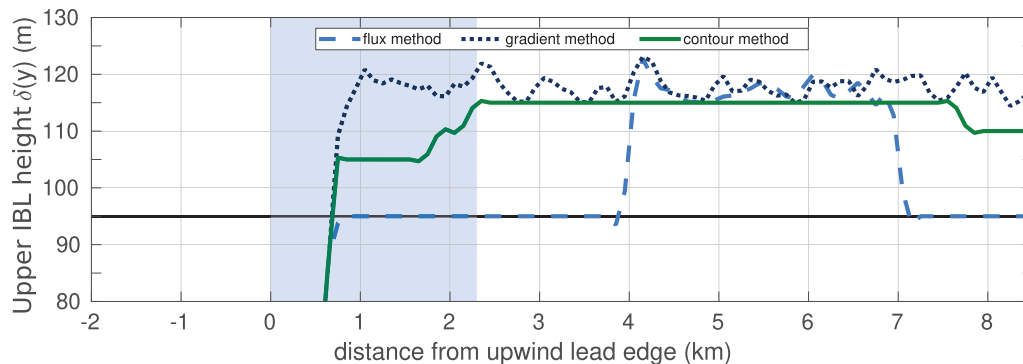


FIGURE 10 Upper IBL height $\delta(y)$ for 10 March 2013 obtained with the M20 parametrization following Equation (11), but a y -dependent ABL height $z_i(y)$ determined by three different methods following Sullivan *et al.* (1998) (see text) is used as upper limit for $\delta(y)$, where y is the distance from the upwind lead edge at $y = 0$ km. For the contour method, $\theta_c = 246.8$ K. The position of the lead is denoted by the shaded rectangle. The upwind observed ABL height is $z_i = 95$ m (horizontal solid black line)

value 2.3 for their parameter a overestimates the observed IBL height, but an improved agreement was obtained with $a = 1.9$. Hence, to include the effect of the positive upwind potential temperature gradient on the growth of the plume over the lead for 25 and 26 March, we consider further simulations for the two stable cases with alternative values for a . We apply the same equation and methods proposed by M20 to determine a (their appendix B), but use the measurements from STABLE instead of LES results.

M20 obtained a by rearranging Equation (11) and calculating open quantities (B_l , D_w , $\delta(y)$ and U) from LES. To determine $\delta(y)$, they applied a linear approximation of LES results in the region $\delta(y) < z_i$. An equivalent procedure is applied here, so that we solve the first line of Equation (11) for a assuming $\delta(y) < z_i$ and obtain

$$a = \frac{\delta_{\text{obs}}^{2/3}(y)}{\frac{2}{3} \frac{B_l^{1/3}}{U} y}, \quad 0 \leq y \leq L. \quad (18)$$

In this equation, δ_{obs} and U can be taken directly from the observations and B_l is determined with measured near-surface temperatures and wind speeds using a bulk formula (e.g., Andreas and Murphy, 1986). By linear approximation of δ_{obs} , a follows from any arbitrary pair of δ_{obs} and y . We found that the variability of a with respect to different positions y was indeed small and the constant values $a \approx 0.75$ and $a \approx 0.9$ for 25 and 26 March represent reasonable approximations. Moreover, this points at a functional dependence between a and the upwind vertical temperature gradient, which is discussed in more detail in Section 6. Both values are still inside the range defined for a in the M20 closure ($a = 1 \pm 0.6$; Section 3.1), but obviously lower than $a = 1.2$ as proposed by M20 for their neutral cases.

5.3 | Model runs 1003-NL2 and 1003-NL3

Additional simulation results using the M20 parametrization including a y -dependent z_i (run 1003-NL2) are shown for the case on 10 March as vertical cross-sections (Figure 11) and as vertical profiles (Figure 12a,c,e,g). In Figure 12b,d,f,h, results of the run 1003-NL3 are shown, where the ratio for $z_{0,l}/z_{t,l}$ was assumed as 100 for reasons explained below.

As Figure 11 shows, the application of a varying z_i (run 1003-NL2) causes much more entrainment, a stronger warming effect, more stable stratification at the lead's downwind edge ($y = 2.3$ km), a stronger destruction of the upwind wind speed maximum, and slightly higher momentum fluxes at $y = 2.3$ km than with the runs 1003-MIX and 1003-NL1. This also causes, to some

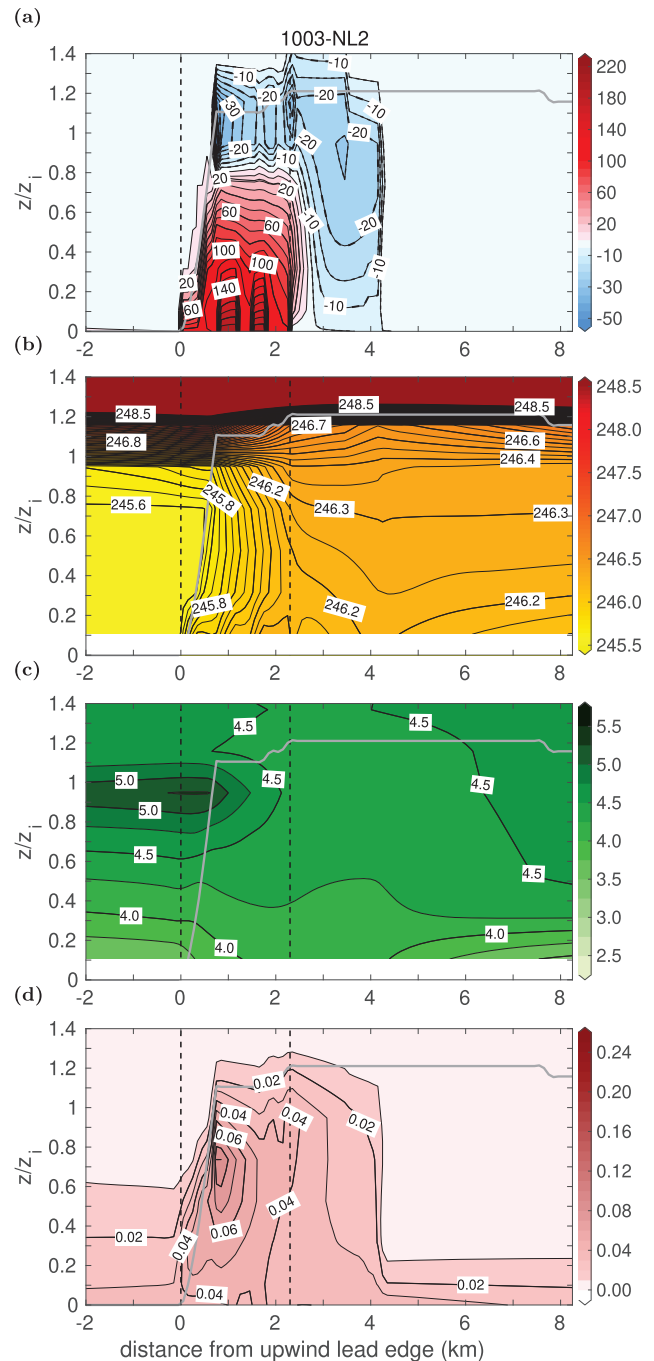


FIGURE 11 As Figure 4, but for the model run 1003-NL2 (Table 1) for 10 March 2013. The upwind observed ABL height is $z_i = 95$ m and for $y > 0$ km a varying upper limit for the upper IBL height (solid grey lines; Equation (11)) is used (Section 5.1)

extent, an improved agreement with the observations (Figure 12a,c,e,g), mainly concerning the temperature profile at $y = 2.3$ km. Comparing this profile with the one at $y = 1.3$ km shows that the stronger vertical entrainment reproduces the observed weakening of the inversion strength over the lead much better than both 1003-MIX and 1003-NL1 (Figure 12c compared to Figure 5c,d). A

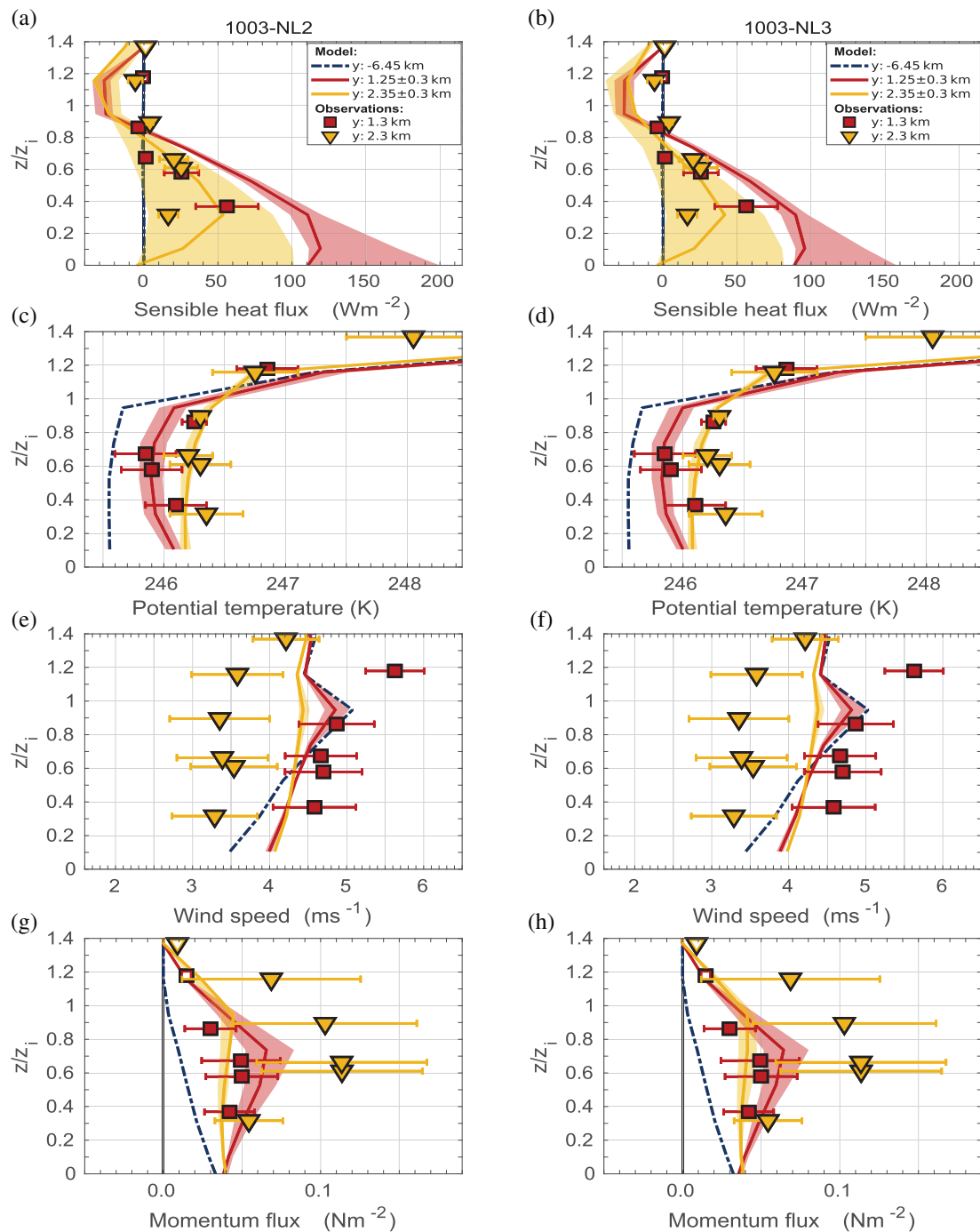


FIGURE 12 As Figure 5, but for runs 1003-NL2 and 1003-NL3 (Table 1) for 10 March 2013. The upwind observed ABL height is $z_i = 95$ m. The lead is located between $y = 0$ km and $y = 2.3$ km

marginal improvement is also obtained for the downwind profiles of both wind speed and momentum fluxes, but also run 1003-NL2 strongly overestimates/underestimates the observed wind/momentum fluxes.

Despite an improvement relative to the runs 1003-MIX and 1003-NL1, run 1003-NL2 also overestimates the observed heat fluxes at the lead's centre ($y = 1.3$ km; Figure 12a). However, as indicated in Figure 12b, this

drawback might be overcome when a lower value of $z_{0,l}$ is applied so that the ratio $z_{0,l}/z_{t,l}$ is strongly increased from 10 to 100 (model run 1003-NL3). Such a large value is still well within the large scatter of observations from other campaigns (e.g., Andreas *et al.*, 2010; Fiedler *et al.*, 2010; Weiss *et al.*, 2011). We consider this as the most realistic explanation for the originally overestimated heat fluxes, but additional factors might also play a role.

5.4 | Model runs 2503-NL2 and 2503-NL3

Figures 13 and 14 show simulated cross-sections and vertical profiles obtained with the runs 2503-NL2 and 2503-NL3 for 25 March, which use the M20 parametrization but with the modifications presented in Sections 5.1 and 5.2. In both runs, the parameter a is lowered to $a=0.75$ and in 2503-NL3, also a y -dependent z_i following the contour method is considered, where $\theta_c = 247.4\text{K}$

is set for the potential temperature contour line (see also Table 1).

The parameter $a=0.75$ in the runs 2503-NL2 and 2503-NL3 causes a more inclined plume (Figure 13a,b), which leads to a horizontal shift of the patterns of temperature, wind, and fluxes (Figure 13a,c,e,g) as compared with run 2503-NL1 with $a=1.2$. Using the y -dependent z_i in run 2503-NL3 causes similar effects as noticed for run 1003-NL2 (10 March; Section 5.3). Due to the much

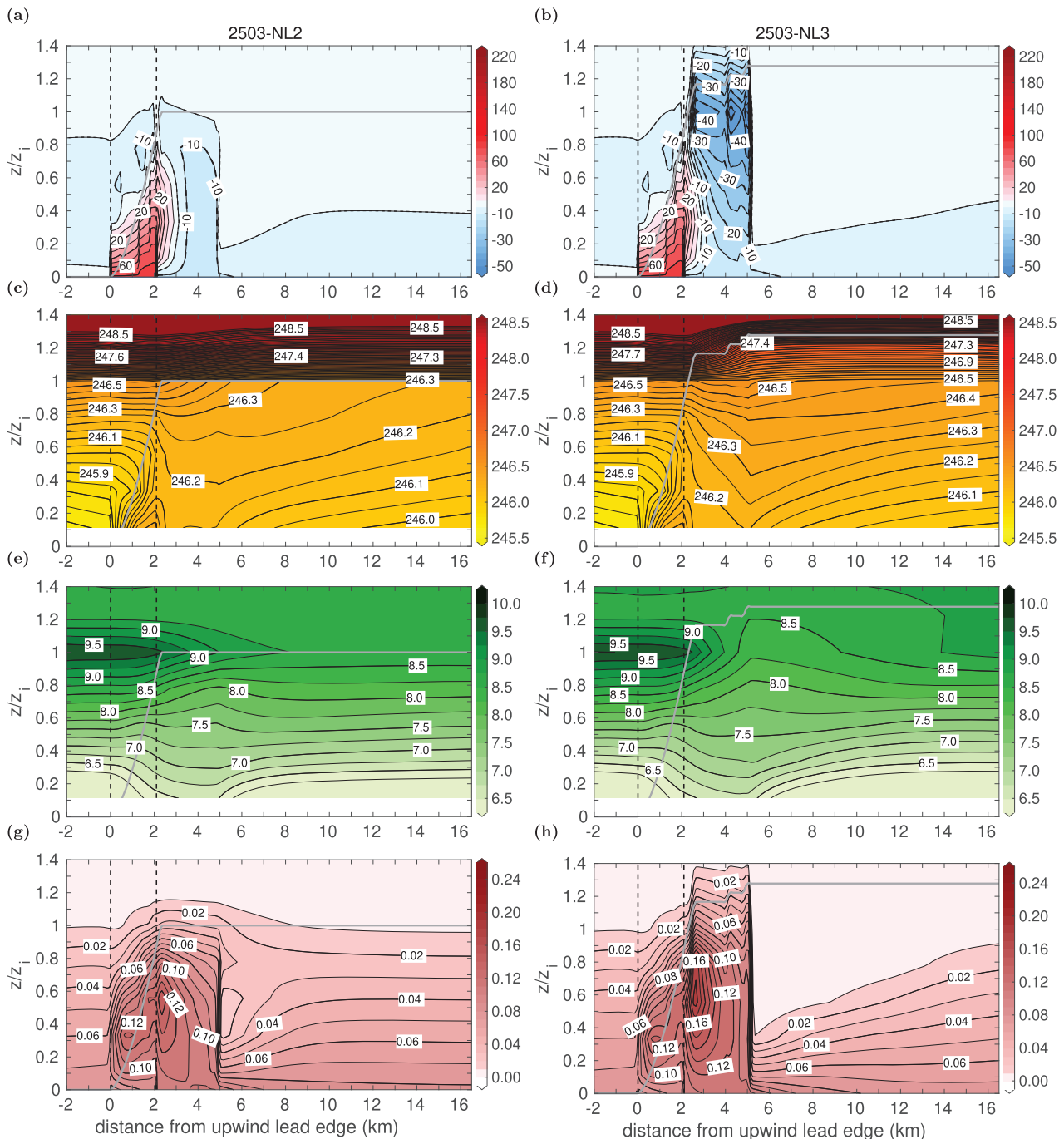


FIGURE 13 As Figure 6, but for the model runs 2503-NL2 and 2503-NL3 (Table 1) for 25 March 2013. The upwind observed ABL height is $z_i = 90\text{ m}$. The set-up of the plots is as described in Figures 4 and 11

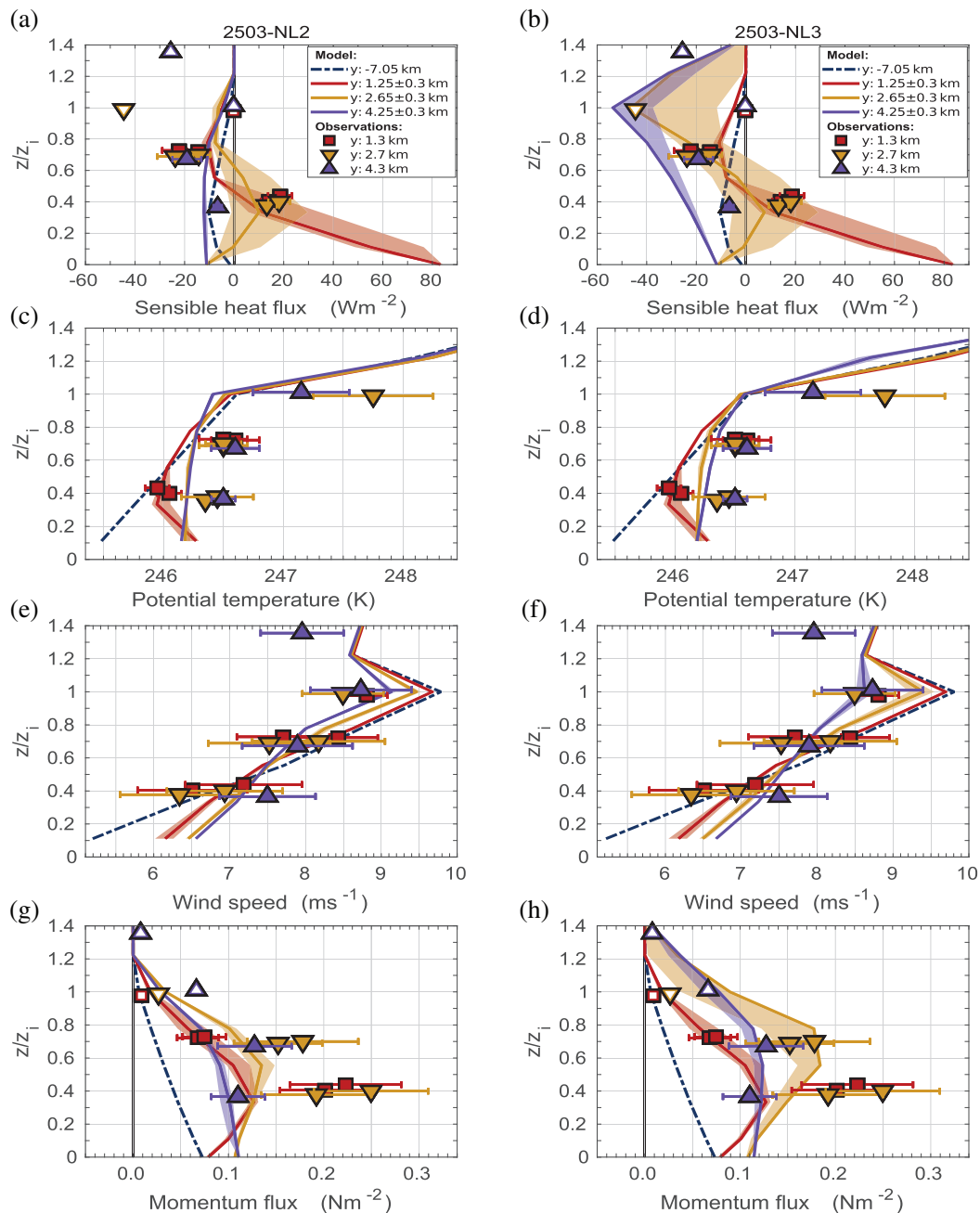


FIGURE 14 As Figure 7, but for runs 2503-NL2 and 2503-NL3 (Table 1) for 25 March 2013. The upwind observed ABL height is $z_i = 90$ m. The lead is located between $y = 0$ km and $y = 2.1$ km. Lines and symbols are explained in Figure 5

stronger entrainment than with 2503-MIX, 2503-NL1, and 2503-NL2, observed temperature and wind patterns (Figure 14d,e) are both better represented, except that the observed regeneration of the wind near $y = 15$ km remains underestimated. Moreover, there is obviously a remarkable improvement for the heat flux in the inversion in the downstream region at $y = 2.7$ km by 2503-NL3, so that entrainment is well captured (Figure 14b). The observed upper plume boundary is also almost exactly reproduced by the simulated monotonic increase of z_i with increasing distance (e.g., Figure 13d).

Despite the strong effect on the entrainment fluxes, the temperature profile simulated by 2503-NL3 shows only slight differences compared to 2503-NL1, but at least a slightly improved representation of the observed ABL warming is achieved, especially at $y = 4.3$ km (Figure 14d). However, the simulated downward flux at that location is much stronger than observed throughout the ABL (Figure 14b). Finally, in the lead's downwind region, the observed decrease of the wind maximum and the observed momentum fluxes are better reproduced by run 2503-NL3 than by all other runs (Figure 14f,h).

5.5 | Model run 2603-NL2

Unlike for 25 March, we show the effects of a lower value for a and a varying z_i in only one simulation (model run 2603-NL2, Figure 15). The lower value for a causes a stronger inclined plume which reaches the inversion further downwind at $y \approx 2.5$ km than in run 2603-NL1. Due to the varying z_i , stronger entrainment fluxes are simulated

(Figure 15a) causing a stronger ABL warming than in run 2603-NL1 (Figure 15c). The effects on wind speed and momentum flux distribution due to the increase in ABL thickness (Figure 15e,g) are substantially the same as shown for the previous cases.

Compared to the observations, the above-mentioned modifications considered in run 2603-NL2 cause improvements relative to runs 2603-NL1 and 2603-MIX,

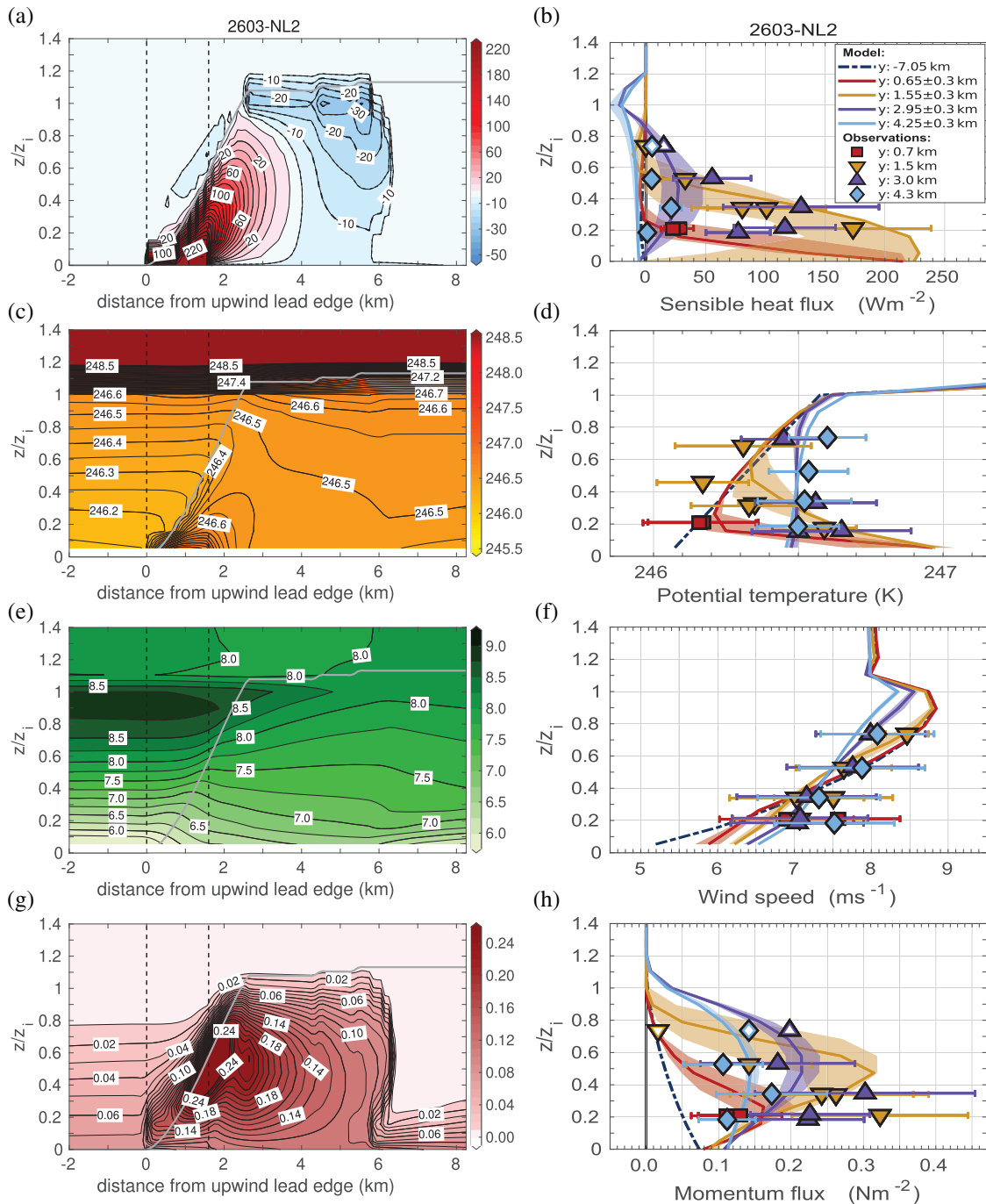


FIGURE 15 (a,c,e,g) are as Figure 8, but for the model run 2603-NL2 (Table 1) for 26 March 2013. The upwind observed ABL height is $z_i = 190$ m. The set-up of the plots is as described in Figures 4 and 11. (b,d,f,h) are as Figure 9, but also for run 2603-NL2 for 26 March 2013. The lead is located between $y = 0$ km and $y = 1.6$ km. Lines and symbols are as explained in Figure 5

mainly concerning flux profiles and temperatures (Figures 15b,d,f,h).

6 | DISCUSSION

Regarding the advantages of the applied non-local closure as compared to the applied local closure, we can formulate two consequences based on our results. First, the quality of agreement between results obtained with the two different closures is more similar than shown by M20 for their idealised cases. This principally also shows that the results obtained with the simple mixing-length closure cannot be completely discarded and that such modelling could be used as a proper rough approximation of (observed) ABL structures over leads. Second, however, when having a closer look at the detailed patterns, we could show that the local closure has some clear limitations. This mainly concerns regions with observed vertical entrainment from the layer above z_i or where the observations hint at counter-gradient transport. At least counter-gradient transport cannot be accounted for in local closures (e.g., L08 and M20) and the parametrization of entrainment would need an additional development for the local closure. The more realistic reproduction of the physical processes over leads related to transport requires a non-local scheme. Moreover, we show that the applied non-local closure can be modified with only a little effort regarding entrainment and plume inclination. Thus, especially by including these two effects, we obtained an improved representation of the observed patterns as compared to the non-modified non-local and the local closure.

The key parameter for a more realistic inclusion of stable inflow conditions turned out to be the parameter a , which is related to the inclination of the convective plume. The values of a used in Section 5 point at a dependence of this parameter from the upwind vertical potential temperature gradient $\partial\bar{\theta}/\partial z$. Obviously, a decreases with increasing $\partial\bar{\theta}/\partial z$. The best fit between these two quantities is obtained by

$$a = b_1 + \frac{1}{b_2 \left\{ 1 + \left(\frac{\partial\bar{\theta}}{\partial z} / \left| \left(\frac{\partial\bar{\theta}}{\partial z} \right)_p \right| \right)^{1/3} \right\}}, \quad (19)$$

where b_1 , b_2 , and $(\partial\bar{\theta}/\partial z)_p$ are constants. Inserting this formulation into Equation (11) would result into a $(\partial\bar{\theta}/\partial z)^{-1/2}$ -dependence of the upper IBL height $\delta(y)$. Such a dependence coincides with the formulations of $\delta(y)$ by, for example, Weisman (1976) and Renfrew and King (2000). The physical meaning of $(\partial\bar{\theta}/\partial z)_p$ becomes clear from the consideration of the denominator in Equation (19). The lower limit for $\partial\bar{\theta}/\partial z$ to obtain a

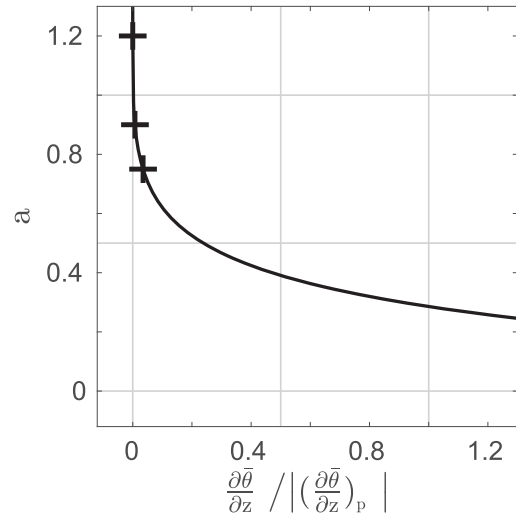
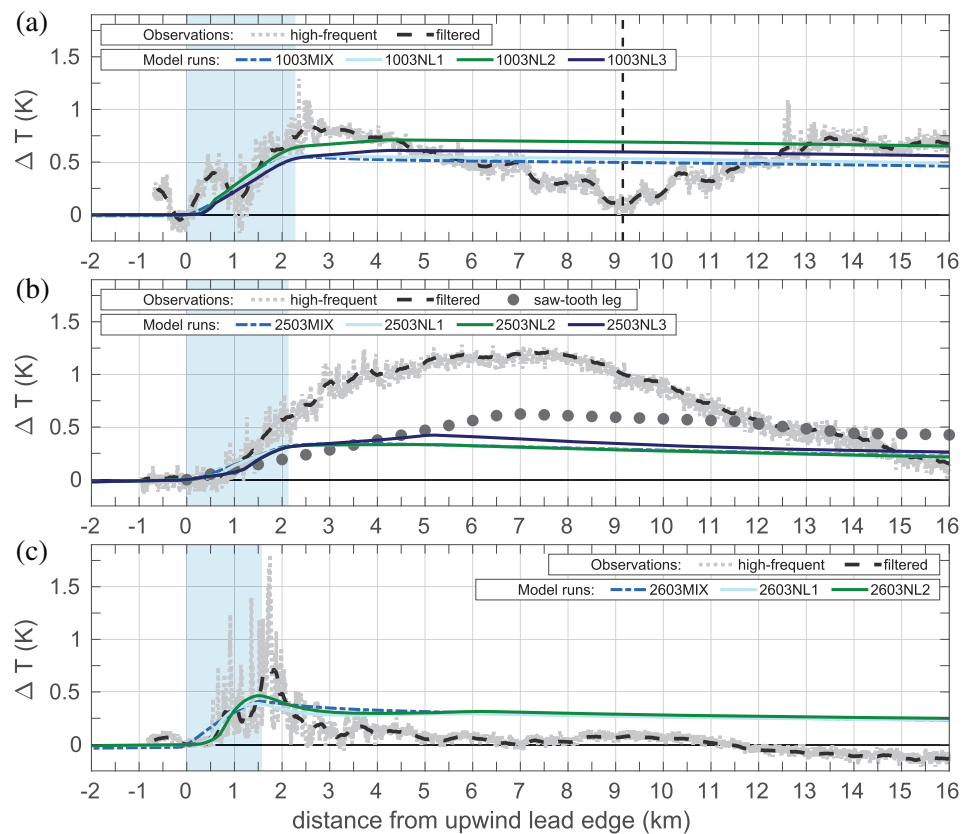


FIGURE 16 Symbols + show parameter a from the M20 parametrization obtained via Equation (18) (based on observed values for all open quantities) plotted against $(\partial\bar{\theta}/\partial z) / |(\partial\bar{\theta}/\partial z)_p|$, where $\partial\bar{\theta}/\partial z$ is the upwind observed ABL-averaged vertical potential temperature gradient (Sections 2 and 5.2 and Table 2). Solid curve shows the hyperbolic fit with Equation 19. The constant $(\partial\bar{\theta}/\partial z)_p \approx -0.41 \text{ K}\cdot\text{m}^{-1}$ (see text)

growing plume ($a > 0$) is exactly $(\partial\bar{\theta}/\partial z)_p$. Considering the values derived for a and $\partial\bar{\theta}/\partial z$ in Section 5.2 and the value $a = 1.2$ for neutral stratification (M20), we obtain $b_1 \approx -0.63$ and $b_2 \approx 0.55$ (Figure 16). With these values for b_1 and b_2 , we obtain $(\partial\bar{\theta}/\partial z)_p \approx -0.41 \text{ K}\cdot\text{m}^{-1}$. Thus, the parametrization (19) does not have any singularity for neutral and stable inflows ($\partial\bar{\theta}/\partial z \geq 0$). Note that the previous formulations of $\delta(y)$ by Weisman (1976) and Renfrew and King (2000) show singularities for neutral conditions. However, we want to stress that the functional relation (19) is based only on three values for $\partial\bar{\theta}/\partial z$. Thus, more cases, either observations or LES runs, are needed in future for a validation. Moreover, the question arises if an alternative version of the parametrization (19) could be derived, for example, based on a dependence of a on the ABL-averaged bulk Richardson number in the inflow region. Further investigation is needed, but our approach can be regarded as a first step, being valid for neutral and stable inflow conditions with a capping inversion.

Simulation results obtained with the non-modified version of the applied non-local closure showed some discrepancies compared with the observations (Section 4). We have shown that they can be partly overcome by applying two modifications introduced in Sections 5.1 and 5.2. Despite an improvement in several aspects, some of the observed features still cannot be reproduced. These discrepancies become more obvious by considering another measure to analyse the overall quality of the applied parametrizations. Namely, we compare the simulated

FIGURE 17 Observed and simulated deviation from the upstream lead edge atmospheric temperature, ΔT (K), along distance from the upwind lead edge for (a) 10 March, (b) 25 March and (c) 26 March 2013. Values are shown for the altitude of the low-level cross-lead flight legs performed on the respective days at 45 m on 10 March and at 35 m on 25 and 26 March (T15). The observed ΔT is shown in high frequency (light grey lines) and as a running mean of approximately 350 m (dashed lines) as also applied by T15 (their figure 4c). The other lines refer to the model results of the respective runs (Table 1). The positions of the leads are denoted by the blue-shaded rectangles. In (a), the vertical dashed black line denotes the position of another crack observed on 10 March, which is not considered in the corresponding model runs. In (b), the dots show ΔT at approximately 35 m height as interpolated from the saw-tooth leg (Figure 1d)



warming of the downwind ABL with the observed one based on results in Figure 17 obtained from low-level horizontal flight sections orthogonal to the leads. The air temperature deviations ΔT between the local air temperature and the temperature at the upwind lead edges ($y = 0$ km) are plotted. In Figure 17b, additional observations are shown based on the saw-tooth leg (Figure 1d). Both curves differ by up to 0.6 K, probably because the saw-tooth and low-level legs have a temporal difference of about 2 hr. The corresponding model runs basically underestimate the warming derived from both observations, where the run using an improved representation of vertical entrainment (2503-NL3) is closest to the observations ($\max(\Delta T) \approx 0.4$ K). This shows that vertical entrainment basically also contributed to the downwind warming, as already stated by T15. However, the large difference between the two observed patterns might be explained by further effects, such as discrete mixing events, which are not captured by the model. Further investigation is needed to show whether this is a unique phenomenon only for this particular case, or if this points at a potential impact of leads in strongly stable environments in general.

For 10 and 26 March, the observed warming effect at the downwind lead edges is well represented by the model runs, especially by those using the M20 closure

including the modifications introduced in Section 5 (runs 1003-NL2 and 2603-NL2 for 10 and 26 March, respectively; Figures 17a and 17c). A discrepancy is shown for the region further downwind, where observed temperatures decreased, while simulated temperatures remain almost constant with increasing distance. This is most probably due to the observed warming of the downwind sea ice surface by the warmer air, which is neglected in our simulations. Besides temperatures, wind and flux profiles might also be affected by this simplification, but further studies including a coupling of sea ice and atmosphere would be needed to prove this.

There is another drawback raising questions which could not be solved so far, namely the observed regeneration of the LLJ downstream of the leads could not be modelled independently on the used closure. This might be related to the difficulties simulating the observed momentum fluxes, which are partly strongly underestimated by the model. For 10 March, this concerns especially the region at the downwind lead edge in the upper half of the ABL and near the inversion layer. Note that for this case, the observed wind speed maximum upwind of the lead was located much higher than in the model results, which at least contributed to the deviation in the momentum flux patterns further downwind for that case. For that

case, we also tested the sensitivity of the model results on z_0 by increasing z_0 by a factor of 10 to $z_0 = 10^{-2}$ m over sea ice downwind of the lead. This increased the momentum flux at the sea ice surface, but it had only negligible impact on model results at higher altitudes so that no real improvement was obtained (not shown).

For 25 and 26 March, the largest deviations between simulated and observed momentum fluxes are found rather in the lower half of the ABL. Regarding the model results obtained with the M20 parametrization, further non-local effects in the momentum transport that are currently not included in the closure might contribute to the deviations. These refer to the inability to simulate maxima in the momentum fluxes on the downstream side of a lead, obtained by LES (M20).

We speculate that the described drawbacks cannot be overcome by simple means, for example, by a local closure of 1.5-order based on the prediction of TKE since we do not see any strong local source for TKE. But a final answer is only possible by implementing and testing different schemes, which requires further research beyond the scope of our study.

Finally, we stress that the measurements from STABLE form a valuable and, to the best of our knowledge, unique dataset for lead-generated convection, but measurement uncertainties of course remain (Section 2). However, as also stressed by T15, the flight patterns had been arranged in a way to obtain reliable turbulent fluxes. Thus, for the evaluation of the model results, we consider the corresponding observed structures as robust. Moreover, the existence of counter-gradient transport in the environment of leads was clearly proven by LES (L08, M20) and the measurements from STABLE at least hint at such fluxes also in nature. The phenomena we described should be studied in future by further measurements and modelling.

7 | CONCLUSIONS

The main goal of our study was to discuss the quality of microscale non-eddy-resolving model results obtained with a local and a non-local turbulence parametrization when compared to airborne observations of the convective flow over leads in sea ice. We focused on results obtained with the non-local closure by M20. It represents a lead width-dependent approach based on LES and is designed for idealised conditions of a lead-perpendicular, near-neutral inflow in an ABL capped by a strong inversion. The applied local closure follows a mixing-length approach.

First, we aimed at identifying advantages of the non-local closure as compared to the simpler local closure. To that aim, we considered three cases from the aircraft

measurement campaign STABLE, where convection over leads was observed over the Arctic MIZ in March 2013. Hence, unlike in previous studies where such analyses were mainly based on comparisons with high-resolved LES data for idealised cases, in this study it was possible to investigate to what extent observations can be reproduced by microscale modelling. The large observational dataset includes high-frequent measurements of temperature and wind components, from which also turbulent fluxes of heat and momentum had been calculated. All cases are characterised by a nearly lead-perpendicular flow in a shallow neutral or stable upwind ABL with a capping inversion at 90 to 190 m over leads of 1.6 to 2.3 km width. The surface temperature of the leads, which were mostly completely covered by nilas, ranged from -17.0 to -5.8 °C on average, in one case with large spatial variations. These observations in connection with upwind measured profiles of wind and temperature were used to initialise the model runs. Then, the model results were compared with measurements from above and downwind of the leads.

With both closures, the basic observed patterns caused by the lead-generated convection were reproduced. This includes the formation of inclined plumes with height-dependent fluxes different to typical flux profiles for convection over homogeneous surfaces. Unlike for the idealised cases by M20, here the overall quality of agreement between the results obtained with the two different closures was more similar. Thus, at first glance, there seems to be no clear advantage of a non-local closure adapted for the inhomogeneous conditions over leads as compared to a simpler local closure. However, a more realistic reproduction of the transport mechanisms over leads clearly requires a non-local scheme since we showed some substantial limitations of the local closure in regions with observed vertical entrainment or where the observations hint at counter-gradient transport.

Second, we investigated the need for further modifications of the M20 parametrization. This was motivated by the underestimation of two observed features, namely entrainment by convection penetrating the capping inversion and a stronger plume inclination as compared to neutral stratification by more stable inflow conditions. Regarding entrainment, we obtained an improved agreement with the observations by accounting for a varying ABL height as an upper limit for the upper plume boundary $\delta(y)$. Furthermore, we postulated a parametrization for the parameter a dependent on the vertical temperature gradient. Its inclusion in the equation for $\delta(y)$ in the M20 closure resulted in a formulation similar to previous parametrizations for $\delta(y)$ by other authors. Unlike these previous formulations, the new one is valid for both neutral and stable inflow conditions although further research is necessary including more measurements in future for validation.

Besides that, some observed features especially related to momentum transport were also still not reproduced by model runs using the modified M20 parametrization.

Altogether, after the first two steps were made by L08 and M20, our study provided another step in the development of atmospheric turbulence parametrizations for non-eddy-resolving small-scale models in a strongly inhomogeneous convective and dry boundary layer. Regarding the non-local closure, we showed that variations in the ABL height and in upwind stability can be considered. A further development should explicitly include moisture transport and the interaction of a warming downwind ABL with the sea ice surface, so a coupled sea ice–atmosphere model. A basic agreement with observed ABL patterns was also obtained not only by simulations using the non-local closure but also with a local closure, at least to some extent. Such model applications as used here might be suitable for future sensitivity studies to study the large-scale impact of leads at low numerical cost, which might help to improve surface flux parametrizations over the MIZ in weather prediction and climate models, where evaluation of selected studies using additional LES or observations might then be needed also. All this would certainly help to give a more detailed picture on the quality of different closure schemes applied in non-eddy-resolving model simulations of a strongly inhomogeneous convective environment.

ACKNOWLEDGEMENTS

We gratefully acknowledge the funding by the Deutsche Forschungsgemeinschaft (DFG, German Research Foundation) project number 268020496 TRR 172 within the Transregional Collaborative Research Center ArctiC Amplification: Climate-Relevant Atmospheric and Surface Processes, and Feedback Mechanisms (AC)3. This work was also supported by the DFG in the framework of the priority program ‘Antarctic Research with comparative investigations in Arctic ice areas’ SPP 1158 (grant LU 818/5-1). We are glad to thank Dr Vladimir M. Gryanik for constructive suggestions and critical comments. We also thank Tim Gollnik for providing subroutines in METRAS for flux calculations and for his support to run the model at the German Climate Computing Centre (DKRZ). Processing of all data and their visualisation were done with MATLAB 2020a. We thank Ian Brooks and two further reviewers for their constructive criticism that helped to improve the manuscript. Open Access funding enabled and organized by ProjektDEAL.

CONFLICT OF INTEREST

The authors declare no conflicts of interest.

DATA AVAILABILITY STATEMENT

The dataset from STABLE is available on PANGAEA repository (Lüpkes et al., 2021). An authorised version of the METRAS code is available on request at University of Hamburg, Germany, see technical report (Schlünzen *et al.*, 2012a).

ORCID

Janosch Michaelis  <https://orcid.org/0000-0002-0564-2083>

REFERENCES

- Alam, A. and Curry, J.A. (1995) Lead-induced atmospheric circulations. *Journal of Geophysical Research: Oceans*, 100, 4643–4651. <https://doi.org/10.1029/94JC02562>
- Alam, A. and Curry, J.A. (1997) Determination of surface turbulent fluxes over leads in Arctic sea ice. *Journal of Geophysical Research: Oceans*, 102, 3331–3343. <https://doi.org/10.1029/96JC03606>
- Andreas, E.L. and Cash, B.A. (1999) Convective heat transfer over wintertime leads and polynyas. *Journal of Geophysical Research: Oceans*, 104, 25721–25734. <https://doi.org/10.1029/1999JC900241>
- Andreas, E.L., Horst, T.W., Grachev, A.A., Persson, P.O.G., Fairall, C.W., Guest, P.S. and Jordan, R.E. (2010) Parametrizing turbulent exchange over summer sea ice and the marginal ice zone. *Quarterly Journal of the Royal Meteorological Society*, 136, 927–943. <https://doi.org/10.1002/qj.618>
- Andreas, E.L. and Murphy, B. (1986) Bulk transfer coefficients for heat and momentum over leads and polynyas. *Journal of Physical Oceanography*, 16, 1875–1883. [https://doi.org/10.1175/1520-0485\(1986\)016<1875:BTCFHA>2.0.CO;2](https://doi.org/10.1175/1520-0485(1986)016<1875:BTCFHA>2.0.CO;2)
- Andreas, E.L., Paulson, C.A., William, R.M., Lindsay, R.W. and Businger, J.A. (1979) The turbulent heat flux from Arctic leads. *Boundary-Layer Meteorology*, 17, 57–91. <https://doi.org/10.1007/BF00121937>
- Badgley, F.I. (1966) Heat balance at the surface of the Arctic Ocean, pp.215–246 in Proceedings of the Symposium on the Arctic Heat Budget and Atmospheric Circulation, Santa Monica, CA. https://www.rand.org/pubs/research_memoranda/RM5233.html
- Bange, J., Beyrich, F. and Engelbart, D.A.M. (2002) Airborne measurements of turbulent fluxes during LITFASS-98: comparison with ground measurements and remote sensing in a case study. *Theoretical and Applied Climatology*, 73, 35–51. <https://doi.org/10.1007/s00704-002-0692-6>
- Batrak, Y. and Müller, M. (2018) Atmospheric response to kilometer-scale changes in sea ice concentration within the marginal ice zone. *Geophysical Research Letters*, 45, 6702–6709. <https://doi.org/10.1029/2018GL078295>
- Brown, A.R. (1996) Evaluation of parametrization schemes for the convective boundary layer using large-eddy simulation results. *Boundary-Layer Meteorology*, 81, 167–200. <https://doi.org/10.1007/BF00119064>
- Businger, J.A., Wyngaard, J.C., Izumi, Y. and Bradley, E.F. (1971) Flux-profile relationships in the atmospheric surface layer. *Journal of the Atmospheric Sciences*, 28, 181–189.

- [https://doi.org/10.1175/1520-0469\(1971\)028<0181:FPRITA>2.0.CO;2](https://doi.org/10.1175/1520-0469(1971)028<0181:FPRITA>2.0.CO;2)
- Chechin, D.G., Makhotina, I.A., Lüpkes, C. and Makshtas, A.P. (2019) Effect of wind speed and leads on clear-sky cooling over Arctic sea ice during polar night. *Journal of the Atmospheric Sciences*, 76, 2481–2503. <https://doi.org/10.1175/JAS-D-18-0277.1>
- Dare, R.A. and Atkinson, B.W. (2000) Atmospheric response to spatial variations in concentration and size of polynyas in the Southern Ocean sea-ice zone. *Boundary-Layer Meteorology*, 94, 65–88. <https://doi.org/10.1023/A:1002442212593>
- Deardorff, J.W. (1972) Theoretical expression for the countergradient vertical heat flux. *Journal of Geophysical Research*, 77, 5900–5904. <https://doi.org/10.1029/JC077i030p05900>
- Deardorff, J.W., Willis, G.E. and Stockton, B. (1980) Laboratory studies of the entrainment zone of a convectively mixed layer. *Journal of Fluid Mechanics*, 100, 41–64. <https://doi.org/10.1017/S0022112080001000>
- Dyer, A.J. (1974) A review of flux-profile relationships. *Boundary-Layer Meteorology*, 7, 363–372. <https://doi.org/10.1007/BF00240838>
- Ebert, E.E. and Curry, J.A. (1993) An intermediate one-dimensional thermodynamic sea ice model for investigating ice–atmosphere interactions. *Journal of Geophysical Research: Oceans*, 98, 10085–10109. <https://doi.org/10.1029/93JC00656>
- Ebner, L., Schröder, D. and Heinemann, G. (2011) Impact of Laptev Sea flaw polynyas on the atmospheric boundary layer and ice production using idealized mesoscale simulations. *Polar Research*, 30, 7210. <https://doi.org/10.3402/polar.v30i0.7210>
- Esau, I. (2007) Amplification of turbulent exchange over wide Arctic leads: large-eddy simulation study. *Journal of Geophysical Research: Atmospheres*, 112. <https://doi.org/10.1029/2006JD007225>
- Fiedler, E.K., Lachlan-Cope, T.A., Renfrew, I.A. and King, J.C. (2010) Convective heat transfer over thin ice-covered coastal polynyas. *Journal of Geophysical Research: Oceans*, 115. <https://doi.org/10.1029/2009JC005797>
- Glendening, J.W. (1994) Dependence of a plume heat budget upon lateral advection. *Journal of the Atmospheric Sciences*, 51, 3517–3530. [https://doi.org/10.1175/1520-0469\(1994\)051<3517:DOAPHB>2.0.CO;2](https://doi.org/10.1175/1520-0469(1994)051<3517:DOAPHB>2.0.CO;2)
- Glendening, J.W. and Burk, S.D. (1992) Turbulent transport from an Arctic lead: a large-eddy simulation. *Boundary-Layer Meteorology*, 59, 315–339. <https://doi.org/10.1007/BF02215457>
- Herbert, F. and Kramm, G. (1985). Trockene Deposition reaktionsträger Substanzen, beschrieben mit einem diagnostischen Modell der bodennahen Luftschicht. In K.H. Becker and J. Löbel (Eds.), *Atmosphärische Spurenstoffe und ihr physikalisch-chemisches Verhalten*. Berlin: Springer, https://doi.org/10.1007/978-3‐642-70531-1_11, (to appear in print).
- Holtslag, A.A.M. and Moeng, C.-H. (1991) Eddy diffusivity and countergradient transport in the convective atmospheric boundary layer. *Journal of the Atmospheric Sciences*, 48, 1690–1698. [https://doi.org/10.1175/1520-0469\(1991\)048<1690:EDACTI>2.0.CO;2](https://doi.org/10.1175/1520-0469(1991)048<1690:EDACTI>2.0.CO;2)
- Li, X., Krueger, S.K., Strong, C., Mace, G.G. and Benson, S. (2020) Midwinter Arctic leads form and dissipate low clouds. *Nature Communications*, 11, 1–8. <https://doi.org/10.1038/s41467-019-14074-5>
- Lindsay, R.W. and Rothrock, D.A. (1995) Arctic sea ice leads from advanced very high resolution radiometer images. *Journal of Geophysical Research: Oceans*, 100, 4533–4544. <https://doi.org/10.1029/94JC02393>
- Lüpkes, C. and Schlünzen, K.H. (1996) Modelling the Arctic convective boundary-layer with different turbulence parameterizations. *Boundary-Layer Meteorology*, 79, 107–130. <https://doi.org/10.1007/BF00120077>
- Lüpkes, C., Hartmann, J., Birnbaum, G., Cohrs, W., Yelland, M., Pascal, R., Spiess, T. and Buschmann, M. (2004). Convection over Arctic leads (COAL). In U. Schauer and G. Kattner (Eds.), *The expedition ARKTIS XIX/1 a, b and XIX/2 of the research vessel POLARSTERN in 2003* Vol. 481, pp. 47–62. Bremerhaven: Alfred Wegener Institute for Polar and Marine Research, DOI 10.2312/BzPM_0481_2004, (to appear in print).
- Lüpkes, C., Gryanik, V.M., Witha, B., Gryscha, M., Raasch, S. and Gollnik, T. (2008a) Modeling convection over arctic leads with LES and a non-eddy-resolving microscale model. *Journal of Geophysical Research: Oceans*, 113. <https://doi.org/10.1029/2007JC004099>
- Lüpkes, C., Vihma, T., Birnbaum, G. and Wacker, U. (2008b) Influence of leads in sea ice on the temperature of the atmospheric boundary layer during polar night. *Geophysical Research Letters*, 35. <https://doi.org/10.1029/2007GL032461>
- Lüpkes, C., Vihma, T., Birnbaum, G., Dierer, S., Garbrecht, T., Gryanik, V.M., Gryscha, M., Hartmann, J., Heinemann, G., Kaleschke, L., Raasch, S., Savijärvi, H., Schlünzen, K.H. and Wacker, U. (2012). Mesoscale modelling of the Arctic atmospheric boundary layer and its interaction with sea ice. In P. Lemke and H.-W. Jacobi. (Eds.), *Arctic Climate Change - The ACSYS Decade and Beyond* (Vol. 43 pp. 279–324). Berlin: Springer.
- Lüpkes, C., Hartmann, J., Schmitt, A. U., Michaelis, J. (2021). Convection over sea ice leads: Airborne measurements of the campaign STABLE from March 2013. Alfred Wegener Institute, Helmholtz Centre for Polar and Marine Research, Bremerhaven, PANGAEA, <https://doi.org/10.1594/PANGAEA.927260>
- Marcq, S. and Weiss, J. (2012) Influence of sea ice lead-width distribution on turbulent heat transfer between the ocean and the atmosphere. *The Cryosphere*, 6, 143–156. <https://doi.org/10.5194/tc-6-143-2012>
- Mauritsen, T., Svensson, G. and Grisogono, B. (2005) Wave flow simulations over Arctic leads. *Boundary-Layer Meteorology*, 117, 259–273. <https://doi.org/10.1007/s10546-004-1427-2>
- Maykut, G.A. (1978) Energy exchange over young sea ice in the central Arctic. *Journal of Geophysical Research: Oceans*, 83, 3646–3658. <https://doi.org/10.1029/JC083iC07p03646>
- Michaelis, J., Lüpkes, C., Zhou, X., Gryscha, M. and Gryanik, V.M. (2020) Influence of lead width on the turbulent flow over sea ice leads: modeling and parametrization. *Journal of Geophysical Research: Atmospheres*, 125. <https://doi.org/10.1029/2019JD031996>
- Monin, A.S. and Yaglom, A.M. (1971) *Statistical fluid dynamics* Vol. 1. MIT Press, Cambridge, MA.
- Overland, J.E., McNutt, S.L., Groves, J., Salo, S., Andreas, E.L. and Persson, P.O.G. (2000) Regional sensible and radiative heat flux estimates for the winter Arctic during the Surface Heat Budget of the Arctic Ocean (SHEBA) experiment. *Journal of Geophysical Research: Oceans*, 105, 14093–14102. <https://doi.org/10.1029/1999JC000010>

- Paulson, C.A. and Smith, J.D. (1974). The AIDJEX lead experiment. In A. Johnson (Ed.), *AIDJEX Bulletin No. 23*, pp. 1–8. Seattle, WA: University of Washington.
- Persson, P.O.G., Ruffieux, D. and Fairall, C.W. (1997) Recalculations of pack ice and lead surface energy budgets during the Arctic Leads Experiment (LEADDEX) 1992. *Journal of Geophysical Research: Oceans*, 102, 25085–25089. <https://doi.org/10.1029/97JC02045>
- Persson, P.O.G., Fairall, C.W., Andreas, E.L., Guest, P.S. and Perovich, D.K. (2002) Measurements near the Atmospheric Surface Flux Group tower at SHEBA: near-surface conditions and surface energy budget. *Journal of Geophysical Research: Oceans*, 107, SHE-21. <https://doi.org/10.1029/2000JC000705>
- Pinto, J.O., Alam, A., Maslanik, J.A., Curry, J.A. and Stone, R.S. (2003) Surface characteristics and atmospheric footprint of springtime Arctic leads at SHEBA. *Journal of Geophysical Research: Oceans*, 108. <https://doi.org/10.1029/2000JC000473>
- Priestley, C.H.B. and Swinbank, W.C. (1947) Vertical transport of heat by turbulence in the atmosphere. *Proceedings of the Royal Society of London. Series A. Mathematical and Physical Sciences*, 189, 543–561. <https://doi.org/10.1098/rspa.1947.0057>
- Renfrew, I.A. and King, J.C. (2000) A simple model of the convective internal boundary layer and its application to surface heat flux estimates within polynyas. *Boundary-Layer Meteorology*, 94, 335–356. <https://doi.org/10.1023/A:1002492412097>
- Ruffieux, D., Persson, P.O.G., Fairall, C. and Wolfe, D.E. (1995) Ice pack and lead surface energy budgets during LEADDEX 1992. *Journal of Geophysical Research: Oceans*, 100, 4593–4612. <https://doi.org/10.1029/94JC02485>
- Schlünzen, K.H., Bungert, U., Flagg, D.D., Fock, B.H., Gierisch, A., Grawe, D., Kirschner, P., Lüpkes, C., Reinhardt, V., Ries, H., Schoetter, R., Spensberger, C. and Uphoff, M. (2012a) *Technical Documentation of the Multiscale Model System M-SYS (METRAS, MITRAS, MECTM, MICTM, MESIM)*. Technical Report 3, Meteorologisches Institut, Universität Hamburg, Germany.
- Schlünzen, K.H., Flagg, D.D., Fock, B.H., Gierisch, A., Lüpkes, C., Reinhardt, V. and Spensberger, C. (2012b) *Scientific Documentation of the Multiscale Model System M-SYS (METRAS, MITRAS, MECTM, MICTM, MESIM)*. Technical Report 4, Meteorologisches Institut, Universität Hamburg, Germany.
- Smith, S.D., Muench, R.D. and Pease, C.H. (1990) Polynyas and leads: an overview of physical processes and environment. *Journal of Geophysical Research: Oceans*, 95, 9461–9479. <https://doi.org/10.1029/JC095iC06p09461>
- Sullivan, P.P., Moeng, C.-H., Stevens, B., Lenschow, D.H. and Mayor, S.D. (1998) Structure of the entrainment zone capping the convective atmospheric boundary layer. *Journal of the Atmospheric Sciences*, 55, 3042–3064. [https://doi.org/10.1175/1520-0469\(1998\)055<3042:SOTEZC>2.0.CO;2](https://doi.org/10.1175/1520-0469(1998)055<3042:SOTEZC>2.0.CO;2)
- Tetzlaff, A., Lüpkes, C. and Hartmann, J. (2015) Aircraft-based observations of atmospheric boundary-layer modification over Arctic leads. *Quarterly Journal of the Royal Meteorological Society*, 141, 2839–2856. <https://doi.org/10.1002/qj.2568>
- Turner, J.S. (1986) Turbulent entrainment: the development of the entrainment assumption, and its application to geophysical flows. *Journal of Fluid Mechanics*, 173, 431–471. <https://doi.org/10.1017/S0022112086001222>
- Vihma, T., Pirazzini, R., Fer, I., Renfrew, I.A., Sedlar, J., Tjernström, M., Lüpkes, C., Nygard, T., Notz, D., Weiss, J., Marsan, D., Cheng, B., Birnbaum, G., Gerland, S., Chechin, D. and Gascard, J.C. (2014) Advances in understanding and parameterization of small-scale physical processes in the marine Arctic climate system: a review. *Atmospheric Chemistry and Physics*, 14, 9403–9450. <https://doi.org/10.5194/acp-14-9403-2014>
- Weinbrecht, S. and Raasch, S. (2001) High-resolution simulations of the turbulent flow in the vicinity of an Arctic lead. *Journal of Geophysical Research: Oceans*, 106, 27035–27046. <https://doi.org/10.1029/2000JC000781>
- Weisman, B. (1976) On the criteria for the occurrence of fumigation inland from a large lake. *Atmospheric Environment (1967)*, 10, 172–173. [https://doi.org/10.1016/0004-6981\(76\)90243-2](https://doi.org/10.1016/0004-6981(76)90243-2)
- Weiss, A.I., King, J., Lachlan-Cope, T. and Ladkin, R. (2011) On the effective aerodynamic and scalar roughness length of Weddell Sea ice. *Journal of Geophysical Research: Atmospheres*, 116. <https://doi.org/10.1029/2011JD015949>
- Wenta, M. and Herman, A. (2018) The influence of the spatial distribution of leads and ice floes on the atmospheric boundary layer over fragmented sea ice. *Annals of Glaciology*, 59, 213–230. <https://doi.org/10.1017/aog.2018.15>
- Zulauf, M.A. and Krueger, S.K. (2003a) Two-dimensional cloud-resolving modeling of the atmospheric effects of Arctic leads based upon midwinter conditions at the Surface Heat Budget of the Arctic Ocean ice camp. *Journal of Geophysical Research: Atmospheres*, 108. <https://doi.org/10.1029/2002JD002643>
- Zulauf, M.A. and Krueger, S.K. (2003b) Two-dimensional numerical simulations of Arctic leads: plume penetration height. *Journal of Geophysical Research: Oceans*, 108. <https://doi.org/10.1029/2000JC000495>

How to cite this article: Michaelis J, Lüpkes C, Schmitt AU, Hartmann J. Modelling and parametrization of the convective flow over leads in sea ice and comparison with airborne observations. *Q J R Meteorol Soc.* 2021;147:914–943. <https://doi.org/10.1002/qj.3953>